Thermal profile and kinetic analysis of Arc–Reactor anode: Finite element analysis

Hannu Heijke Out

Thesis submitted in partial fulfilment
of the requirements for the degree of
ME

Department of Chemical and Process Engineering, University of Canterbury

2014

Acknowledgements

This thesis would not have been possible without the support and encouragement of many. From Dr. John Abrahamson without whom this work would never have started, whose enthusiasm and support made this possible. Dr. Aaron Marshall my supervisor for his advice and considerable patience, Assoc Prof. Ken Morison whose energetic guidance greatly advanced my modelling ability.

To the CAPE technical staff for there advice and assistance with any questions or modifications. To the staff of Arcactive for a friendly and helpful workplace. To Grisha for advice and guidance, Shane and Euan for light–hearted stress relieving conversation. To my family and friends for continued support.

Abstract

This study investigated the heat transfer within the anode material moving through and heated by an electric arc. The arc was a low current ($<$ 16 A) atmospheric electric discharge between a carbon rod cathode, and a moving carbon felt anode. The carbon arc was a low current($<$16 A) electric discharge between a cathode constructed of a carbon rod, and a moving carbon felt anode.

The thermal profile within the anode material was predicted by a system of differential algebraic equations, adapted from the model developed by (Stark and Fricke, 1993). This set of equations was run using the software MATLAB R2011b, using a numerical integrator with consideration taken for sparsity.

The change in degree of graphitisation was then predicted using the thermal profiles developed. This indicated that while the graphitisation of the surface of the felt exposed to the arc increased (from about 10% to about 99%) this effect did not penetrate far into the felt. At a depth of 0.3 mm there was very little increase in graphitisation (about 7% increase at slow movement rates, negligible at standard rates), indicating that this gaphitisation degree was unlikely to explain the improvement of battery cells produced using this material compared to non–arc treated material.

Vaporisation of carbon due to the arc was then investigated as a possible explanation. With a similar activation energy to graphitisation a similar profile was obtained.

Contents

List of Figures

List of Tables

0.1 Nomenclature

λ_D	Deybe length
κ	Boltzmann constant
ε_0	permittivity of free space
e	electron charge
T	Temperature
n_p	density of positive ions
r	radial distance from point charge
V	potential due to point charge
L	size of plasma
j	charge
v_e	average velocity of electrons
v_i	average velocity of ions
m	mass of electron
u	root mean square velocity of random electron motion
X	electric field
E_e	energy of excited atom
E_i	energy of ionized atom
W	work
t	time
u_i	vector of dependent variables at position i
ε	emissivity
λ	wavelength
F	force
g	acceleration due to gravity
V	volume
ρ	density
Ra	Rayleigh number
β	coefficient of volume expansion
C_p	specific heat
K	permeability of solid skeleton
μ	dynamic viscosity
k	apparent thermal conductivity
R	resistance to electric current
I	current
V	voltage
Z	impedance
σ	resistivity
q	heat flux
Z	fibre orientation parallel to heat flux

0.2 Abbreviation

Chapter 1

Introduction

"On important topics it is better to be a good deal prolix than even a very little obscure." Edgar Allan Poe

1.1 Objectives

The ArcActive electrode for a lead-acid battery is constructed from a "arc-treated" material. This "arc-treatment" changes the physical and chemical structure of the carbon material, both internal and external.

The carbon electric arc discharge is a process by which ArcActive treats carbon felt. This treatment is vital to the performance of the carbon material as an electrode in a lead acid battery. This arc discharge is able to be performed in atmospheric conditions, at moderate operating speeds, and with low costs; making the processing of a carbon material into a battery electrode commercially viable.

The physical changes that occur include a greatly reduced electrical resistivity, of about one order of magnitude. It is known that heat treating polyacrylonitrile (PAN) fibres reduces resistivity (Sauder et al., 2001), and this change is linked to temperature and residence time. Therefore this study will focus on the thermal profile in the anode substrate during and after a carbon electric arc discharge.

The objective of this study is to understand the heat treatment that occurs due to the electric arc. That is the temperature profile through the material, and how this changes over time. Due to the high temperatures encountered, it is not possible to physically measure this profile, hence a

mathematical model to track changes during the arc process is required . Due to the complexity involved this will not be an analytical model, but solved by the numerical method known as "method of lines".

1.2 Carbon Electric Arc

On the 20th of March 1800 Volta wrote his first letter announcing his "pile", the first battery. As this naturally preceded ammeters electric current was shown via the creation of a spark. By October Sir Humphry Davy had found two carbon electrodes produced a very acceptable arc (Chaney et al., 1935).

In 1812 Davy conducted a public demonstration of the illuminating possibility of the carbon arc.

An arc occurs when a gas breakdown occurs, after which the normally insulating gas becomes a highly conductive plasma. This form of this plasma depends highly on the means of production, such as the pressure and composition of the gas, the material used for the electrodes, the geometry of the electrodes, and the magnitude of the current flow (Somerville, 1959).

There is however sufficient similarity under a wide range of conditions such that discharges have in common many important characteristic features. They are all given one name, arc discharge. This can occur at currents of 10^{-1} to 10 A, with the name arc usually applied to stable or quasi stable discharge, a spark being used otherwise.

For current to pass between electrode three things required

1. The current must be conducted through the body of the gas. For this to be possible the normally neutral gas must be rendered conducting by the introduction of charged carriers, or by their creation within it, or both.

2. the current mus be transferred across the gas–anode junction

3. the current must be transferred across the cathode–gas junction

In a long arc there are three distinct regions, corresponding to above criteria. These are the conducting column or channel in the gas whose properties are not much influenced by the process occurring at the electrodes. This is often called the positive column.

The anode fall is the region close to the anode surface, typically with 1–10 Debye lengths (Sanders and Pfender, 1984). Over this short distance there is a very rapid voltage drop from the

positive column to the anode. The erosion of the anode is governed by the voltage fall in this region(Hemmi et al., 2002).

A similar effect is observed at the cathode, called the cathode fall region.

1.2.1 Initiation methods

There are three common methods of arc initiation. They work by breaking down the gas between the two electrodes into a electrically conducting pathway.

1. Glow to arc transition.

   In this method the electron transfer starts as thermionic emission at high potentials and low currents. As the current is increased the voltage at first rises, then decreases to a plateau value at which point the gas has transformed into a highly conductive plasma. The current starts at value as low as 10^{-1}A.

2. Spark breakdown.

   An arc is created via a transient non–steady spark discharge. High potentials are applied, which results in the breakdown of the gas causing a spark. The plasma created by this spark is used as the electrical pathway for a arc discharge. The disadvantage of this method is that if the spark voltage is too low an arc is unable to be created. However this does not require moving parts.

3. Electrode retraction.

   In this method the cathode and anode are brought into contact with each–other. When the distance between these electrode is of the order of 1μm (Llewellyn-Jones, 1966) breakdown of the gas occurs resulting in an arc discharge. This is the most common method as high potentials are not required. This can occur in mechanical switches, as current is stopped by withdrawing electrical contacts apart.

1.2.2 Plasma

The arc between two electrodes consists of a plasma. Plasma is often described as the fourth state of matter, along with gas, liquids, and solid phases. Plasma can be broadly defined as being a collection of equal numbers of positive and negative charge carriers, which has a net zero charge. Differing from gases in that the components are charged.

Approximately 99% of the universe exists in plasma form (Nasser, 1971), including many everyday uses. From fluorescent lamps, through to spark–plugs in internal combustion engines.

The conditions for the existence of a plasma can be described by the Deybe length. This is the distance at which the electric field due to one particle is shielded by the particle surrounding it.

$$\lambda_D = \left(\frac{e\varepsilon_0 \kappa T}{n_p e^2} \right)^{1/2} \tag{1.1}$$

$$V = -\frac{e}{4\pi\varepsilon_0 r} \varepsilon^{-r/\lambda_D} \tag{1.2}$$

where

κ = Boltzmann constant

ε_0 = permittivity of free space

e = electron charge

T = Temperature

n_p = density of positive ions

r = radial distance from point charge

V = potential due to point charge

Without this shielding plasma would lose electrons faster than positive ions owning to the higher electron velocity, this would result in loss of neutrality. Hence a plasma can only exist if physical size of the plasma is much greater than the Debye length,

$$L \gg \lambda_D$$

electric field applies force parallel to field of each electron, results in the superposition of a component of velocity parallel to the field so that the mean velocity is no longer zero, but is equal to the drift velocity

$$j = n_e e v_e + n_i e v_i \tag{1.3}$$

Where j is charge in A cm^2, v_e and v_i are average velocities of electrons and ions respectively , e is charge in coulombs, n is the number.

Electron mean free path is

$$v_e = 0.815 \times 10^{-7} \frac{Xel}{mu} \tag{1.4}$$

Where l is mean free path length, m is the electron mass, u the root mean square velocity of random electron motion, X the electric field.

combining give

$$j_e = 0.815 \times 10^{-7} \frac{X n_e e^2 l}{mu} \tag{1.5}$$

with j_e/X may be called the conductivity of the gas due to the electrons, a function of field strength X.

(Llewellyn-Jones, 1966) (Townsend, 1910)

Kinetic energy of an electron $\frac{1}{2}mu^2$ in collision with a neutral gas molecule, if it exceed ionization potential then ionization will occur. Can also occur with partially excited atom,

$$\frac{1}{2} > E_i - E_e \tag{1.6}$$

where E_i is ionization energy, and E_e is excited energy. If E_e is metastable, that is very stable compared to normal excited atom, then rate of ionization is proportional to square of current.

1.3 Material forms

The requirements of the carbon material that could be used for the anode in the carbon arc are limited. The following requirements must be met;

1. Electrically conductive
2. Sufficiently strong to be able to be pulled through the reactor. This equates to the order of 1–2 N mm^{-1} across the width of the material
3. Low cost, a necessity in most process lines
4. Stable at high temperatures. It is expected that the material will be greater than 2000 °C over most of the depth, and up to 3500 °C next to the arc

The materials that best met these requirements were polyacrylonitrile(PAN) derived carbon textiles. As these are based on PAN a (common textile in itself)(Bashir, 1991), the cost is low. The strength and electrical conductivity are increased by the oxidation and carbonisation process described in detail in section 1.4. The carbon fibres derived from PAN are commercially available in many diameters, from 5 μm up to 30 μm. These can be processed into a textile in much

the same way as PAN itself, with some manufactures forming textiles before carbonisation, and some after.

To understand the heat flow through a material it is necessary to understand the material itself. A description is given here of the different forms into which carbon fibre can be processed. *Woven* fibres can be categorised into three different weave types, Twill, Plain, and Satin. This is based on the fabric structure, which is described by the interlacing role of the warp and weft tows (Oelsner, 1953). The tow can be called a tow, yarn or thread by different users, and tow will be used in this text. Tows running lengthways along the cloth are called the warp tows, and those running crossways and carried by the shuttle are the weft tows. The movement of the shuttle above and below the weft thread is what gives a weave its characteristics. The warp tow lying above the weft tow is called the float.

The simplest weave is the plain weave as this is the easiest to pattern, but it is also that which requires the most floats. The plain weave is balanced, which means that the warp and weft come to each face to the same extent. See figure 1.6 for an example of plain weave carbon fibre fabric. This results from the shuttle passing above then below adjacent weft threads, while the float of two adjacent warp threads are never on the same weft thread. The repeating pattern of the weave covers two warp and two weft tows. The size and pattern of this unit cell can be used to classify the weave (Zheng et al., 2009).

The next weave is the twill. A characteristic of the simplest form of the twill weave is that the float of each weft thread is set one warp thread to the right or left of the float of the preceding weft thread. By this process ribbed lines are formed, running in a diagonal direction. See figure 1.5 for an example of twill weave carbon fibre fabric. Twill threads are named by the number of threads covered by each float, likewise for the weft threads. For example denim is typically 2/2 twill, indicating that the warp thread covers two weft threads before passing through, and similar for the weft.

The final weave is the satin weave. The satin weave lacks the distinct diagonal line distinctive to the twill weave. The float of a satin weave will pass over multiple weft tows, however no two adjacent floats will start on the same weft thread. This produces a fabric with a smooth, lustrous face on the cloth. See figure 1.1 for an example of a satin weave.

Fabrics need not be woven; the easiest and simplest method to create a fabric from fibres is to *felt* it. A felt is made by combining a “web” of fibres; this is a large sheet of fibres which can have any orientation. The fibres need not be arranged in a tow. The traditional method for making a felt from wool involves washing it, then laying the washed web out in the desired shape. This web is then beaten till it mats, giving a strong felt fabric. The modern method is the

Figure 1.1: Example of a satin weave

same, except vibrating belts are used rather than a stick. The strength of a felt is often due to the contact friction between fibres of different orientations. However this can be a physical bond as explained below on page 9.

The web can be produced via two different methods. The first is the traditional *carding* process. This involves running the fibres between two rotating cylinders. These cylinders are covered with small flexible wires which tease the fibres out, pulling them in-line with the direction of rotation. This action will also spread the fibres evenly, giving a uniformly aligned web. The other method arrives at a randomly orientated web, giving a felt of uniform strength in all directions. This method involves slowly feeding the fibres into a rapidly moving air stream; the fibres are then carried by the air and deposited onto a screen. By this method a web of random orientation and desired thickness can be created.

The web or webs are then combined into a batt. The number of webs combined gives the thickness of the final felt fabric, the orientation of which provides the strength. By aligning the webs in the same direction, greater strength is achieved in the carded direction; at the detriment of that in the cross direction. The final use of the felt dictates the arrangement, the balancing of the relative strengths.

There are five common methods for felting a fibre (Hollen and Saddler, 1965),

1. Needle punching
2. Solvent bonding
3. Heating
4. Printing
5. Padding

The first method that is used to create carbon fibre felts is needling. Developed in the 1950's this method results in a strong coherent felt. First the fibres are passed through a carding stage to align them, although this step is not necessary. The carded fibres are then combined into webs. These webs are then combined into a batt, with the web number and orientation as desired.

Once in a batt the fibres are then needled. This involves passing the batt under a plate covered with many barbed needles. This plate vertically reciprocates, with the barbs pushing some fibres down through the batt. Below the batt is a bed–plate with hole to accommodate the batt, similarly above the batt is a stripping plate to ensure no fibres are pulled out and above the batt. The batt is moved when the needles are retracted, resulting in a line of needled holes in the machine direction of the felted product shown in figure 1.2.

Figure 1.2: Image of PAN felt

The degree to which the material is self bonded is controlled by the shape, and number of needles, and also the speed and number of passes through the needler. As of 1965 over 160 different needle types were available, to accommodate different fibres and desired rates and final densities.

A study was conducted by Gårdmark and Mårtensson (Gårdmark and Mårtensson, 1966) to evaluate the effect of needling on felt properties. It was found that the strength and density of the felted fabric increased with increased needling, up to a point at which the damage due to the needles became dominant over the increased coherence. See figure 1.3 for the effect of needling on strength, and figure 1.4 for the effect of needling vs density. The absolute values are not of importance, rather the trend is relevant. Also countering the increased coherence is the effect that the weight per unit area decreases due to each needling pass, due to fibre loss from breakages, and the spreading of the felt (increased surface area after needling). Note that the felt is over twice as strong perpendicular to the machine direction as in it. This is likely due to needles progression in a line in the machine direction, while the spacing is set in the perpendicular direction.

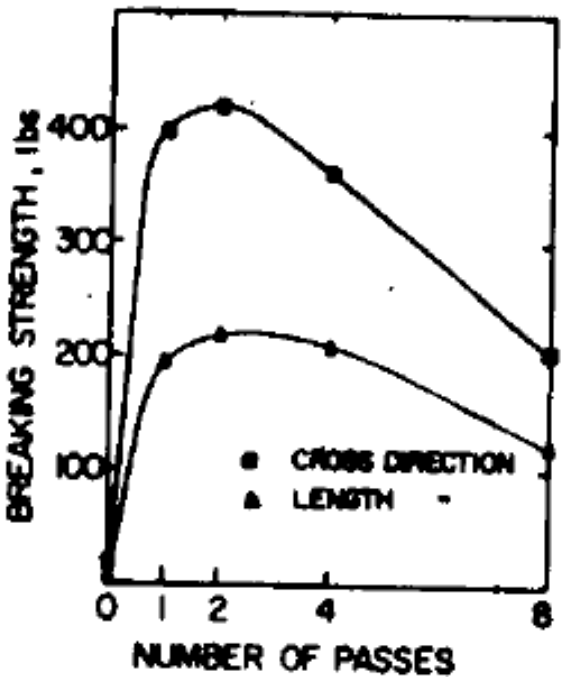

Figure 1.3: Breaking strength as function of the number of passes through the loom

Figures 1.5,1.6, and 1.7 show the three main anode materials used in this study. They represent twill weave, plain weave, and needled felt respectively.

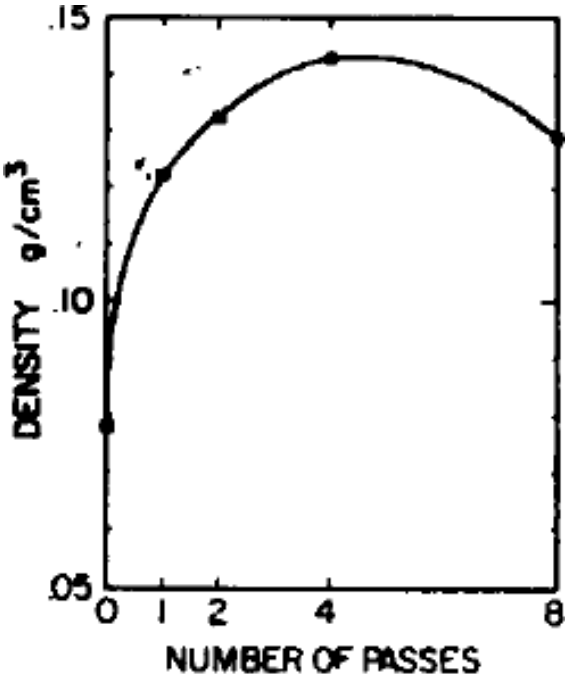

Figure 1.4: Relationship of density to number of passes under the needling zone

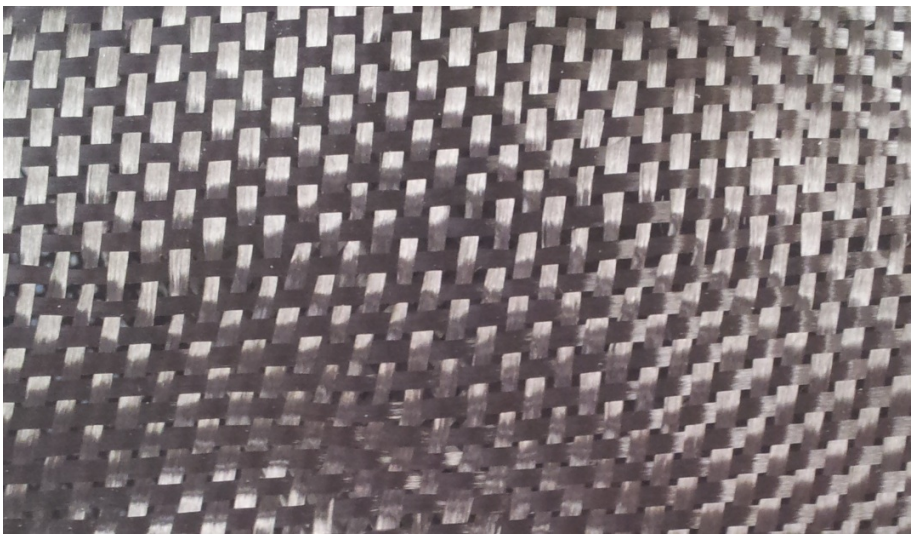

Figure 1.5: Twill weave carbon fibre fabric

Solvent bonding is as the name suggests. A solvent which will partially dissolve the fibres is added to the batt. This is then compressed. The solvent will tend to wick to contacts between fibres, these points then dissolve, and as the solvent evaporates these contacts then become the same material. This creates a very strongly bonded felt; however this method is not usable for all types of fibres. This method is not used with PAN products, however it is viable.

Figure 1.6: Plain weave carbon fibre fabric

Figure 1.7: Needled carbon fibre felt

Heating as a felting method is limited to thermally active fibres, those that have reduced stiffness with increased temperature. The batt is compressed under such heat required to weaken but not

melt the fibres; it is then cooled retaining the hot shape. Often thermoplastic fibres will be added to the web if the desired fibre is difficult to felt, as these will form a rigid matrix giving the felt coherence. This method can be used with some success with natural fibres such as wool. Wool thermosetting is called calendering.

Du Pont produce synthetic fibrous particles called fibrids. These are $1/16$ to $1/36$ of an inch long, with twig like projections. Made from thermoplastics these hold the web together until thermosetting by the above method.

Printing is as the name suggests. Stripes are printed onto the web, and these enable the material to be felted.

Padding is a method by which the felt is supported by a matrix of a bonding compound. The batt is run through a bath containing a liquid emulsion, and then run through a padder. This padder improves the penetration of the emulsion, and removes any excess. This liquid is then set, creating a bonded matrix about the fibres. As of 1965 over 200 different types of bonding agent were used (Hollen and Saddler, 1965). These include a wide range of materials from starch to glues, casein, thermoplastic, and thermosetting resins.

1.3.1 Carbon fibre forms

Carbon fibres are currently produced from three major precursors polyacrylonitrile (PAN), hydrated cellulose (HC), and residual products from refining oil and coal (pitch) (Azarova and Kazakov, 2011). These all have advantages and disadvantages.

Hydrated cellulose as a precursor has a very low yield. For each kg of carbon fibre 8 kg of precursor is required, compared to a ratio of 1:2 for pitch and 1:3 for PAN. HC also produces average carbon fibres, in terms of yield strength and elasticity (see table 1.1). While pitch has the highest yield it has serious drawbacks; pitch is carcinogenic and requires complex treatment before spinning.

	Yield strength [GPa]	Elastic modulus [GPa]
Pitch	1.5-3.0	150-950
PAN	3.5-6.1	230-590
HC	0.4-2.5	30-100

Table 1.1: Carbon fibre properties (Azarova and Kazakov, 2011)(Perepelkin, 2002)

Since the early 2000's when carbon fibres became economically viable compared to glass fibres PAN has come to be the dominant precursor from which carbon fibres are produced, account-

ing for about 90% of the market (Rahaman et al., 2007). Carbon fibre usage worldwide has increased rapidly in recent years, and this is shown in figure 1.8. Research into pitch fibres is still continued. HC fibres are used for the manufacture of gaskets, due to their pliability and high thermal stability.

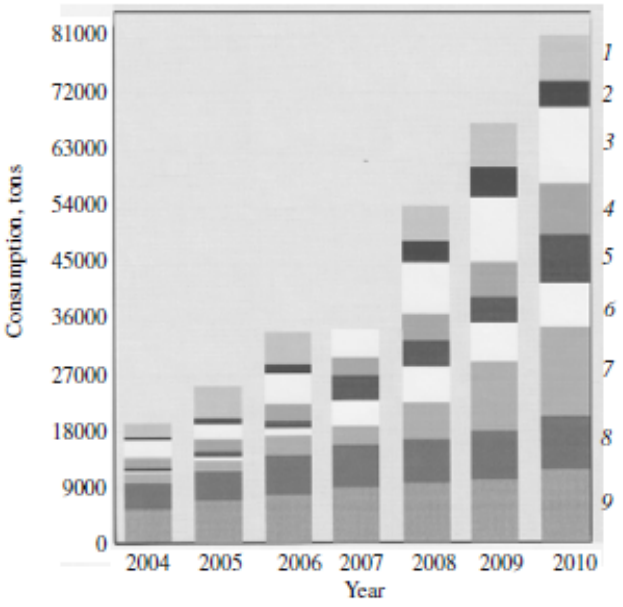

Figure 1.8: World consumption of carbon fibres: 1) thermoplasts (electronics); 2) transportation (including ship building); 3) industry; 4) infrastructure; 5) automobile construction; 6) oil rigs; 7) alternative energy (wind power); 8) sporting goods; 9) aviation and rocket construction. (Azarova and Kazakov, 2011)

1.4 P.A.N Production

PAN fibers were first produced commercially in 1949, by DuPont de Nemours at a pilot plant in Camden (U.S.A) with a capacity of approximately 3000 tons per year. This was based on the work of Rein at I.G. Farbenindustrie and Houtz at DuPont de Nemoures. The process was discovered independently by these two groups within two months of each other in 1942.

PAN is soluble in dimethylformamide with formation of concentrated, relatively stable spinning solutions. Wet and dry spinning produced fibres with good textile properties, in some cases superior to wool. According to international indexing of chemical fibres ISO/TC 38/SC-N1631, 1995, fibre materials whose polymer substrate contains more than 85 wt.% acrylonitrile units are defined as polyacrylonitrile fibres, and those containing $35-50$ wt.% acrylonitrile units are defined as modacrylic fibres. For fibres of $85-92$ wt.%, methyl acrylate and methyl methacrylate,

viny acetate esters are used as the co–monomer to give elasticity, as required for processing.

When the content composed of ester groups is greater than 8 wt.% the flexibility of the macromolecules increases (Kirizbaeva et al., 1981) also resulting in a decrease in glass transition temperature and an increase in elasticity.

The size of a fibre is measured in the unit of tex, where 1 tex = 1 gramme for 1 km of fibre. For PAN fibres it is possible to produce fibres as small as 0.02–0.05 tex. For PAN 10μm diameter is 0.093 tex. Fibres are spun from solution via spinnerets, and spinning occurs at $160-190$ °C under $3-7$ MPa pressure at a speed of up to 6.5 kg hr^{-1} (Luo et al., 2012) per fibre. Figure 1.9 shows an SEM image of the SGL felt used in this study.

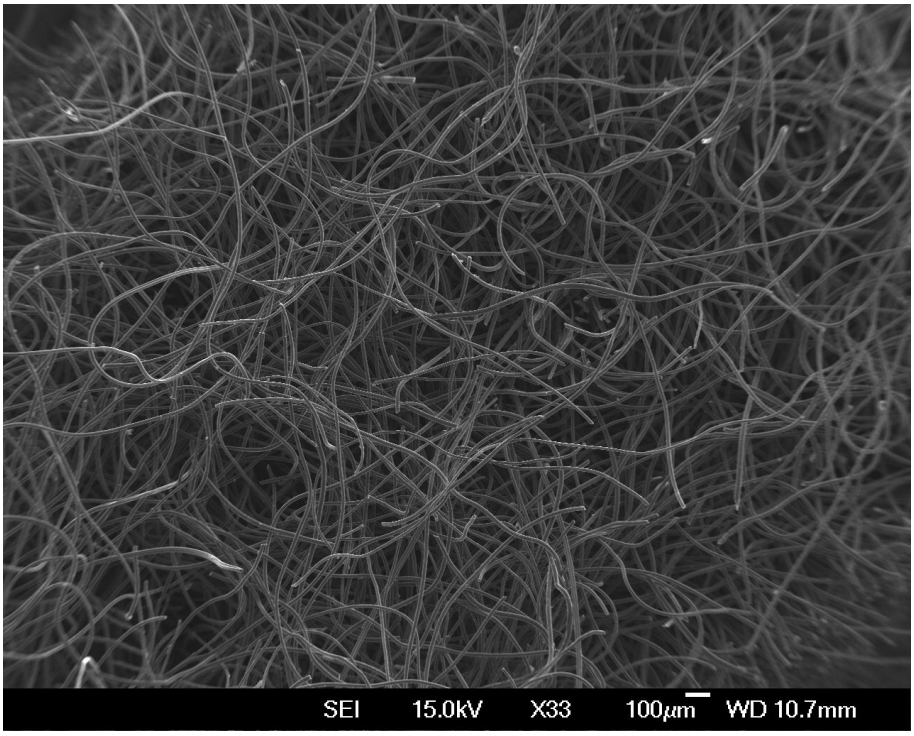

Figure 1.9: SEM image of SGL felt at 33$\times$zoom

Chapter 2

Modelling

2.1 Objective

The aim of this work was to develop an understanding of the heat transfer occurring within the anode material, during passage of the anode attachment of the carbon electric arc, as described in section 3.6 on page 43. The system described is that of a low current carbon electric arc operating at atmospheric pressure in a low oxygen environment. The anode material utilised is a PAN based carbon felt, which is then used as a crucial part of the ArcActive battery. It was thought that the graphitization of the carbon felt is of significant importance to the excellent performance of this battery.

The model that was developed enabled the prediction of history of the heat treatment of the anode material. This was then used with the kinetic data as described in section 2.5.1 to track the expected degree of graphitization for elements of the anode material.

2.2 Implementation

The set of equations described in section 2.4 is a system of partial differential equations, along with many algebraic equations. To solve the system a integration solver is used in MATLAB R2011 b, see section 2.2.3. The system is solved using the method of lines, described further in section 2.2.2. For the sake of calculation speed a sparsity matrix of the form of a Jacobian matrix was used, see section 2.2.4. The effect of this was to greatly reduced the time taken to find the solution; by a factor of about 300, discussed further in section 4.3.

2.2.1 Differential equations

Equations which describe physical properties are inevitably of the form of partial differential equations (PDEs). This is due to the aim of these equations, which is to describe the change of a property in relation to a independent variable, within the four dimensions of space and time. While one can often reduce this number via certain assumptions, it is rarely possible to reduce this down to one dimension.

A PDE is defined as a differential equation with more than one independent variable. If the equation has only one independent variable it is generally termed an ordinary differential equation (ODE) (Schiesser and Griffiths, 2009). An example of a PDE is equation 2.17, which gives the variation of energy E, with space and time. A general example of a first order PDE is given in equation 2.1.

$$\mathrm{W}_t = f(u), \qquad t > 0 \tag{2.1}$$

where
$\mathrm{W}_t = \frac{\partial u}{\partial t}$
u = vector of dependent variables
t = initial value independent variable
f = spatial differential operator
$= f(t, u_1, u_2, ...)$

2.2.2 Method of lines

The method of lines is a computational approach for solving a PDE problem of the form of equation 2.1, that proceeds in two separate steps (Wouwer et al., 2001).

The basic idea is to replace the spatial boundary-value derivatives in the PDE with algebraic approximations (Schiesser and Griffiths, 2009). Once this is done the spatial derivatives are no longer stated explicitly in terms of the spatial independent variables. Thus in effect only the initial value variable (typically time in a physical problem) remains. With only one remaining independent variable we have a system of ODEs that approximates the original PDE. The method of lines uses well established numerical methods for solving the ODEs.

The PDE can be replaced with either a forward equation 2.2, equation central 2.3, or backward equation 2.4 difference approximation. These are Taylor series type numerical approximations to the PDE, approximating using the gradient in the relevant direction. The subscript i denotes

the segment position, *i*+1 represents the segment next to *i* in the forward direction, and vice versa for *i*-1.

$$\text{Forward:} \qquad \frac{\partial u_i}{\partial t} = \frac{u_{i+1} - u_i}{dx} \tag{2.2}$$

$$\text{Central:} \qquad \frac{\partial u_i}{\partial t} = \frac{u_{i+1} - u_{i+1}}{2dx} \tag{2.3}$$

$$\text{Backward:} \qquad \frac{\partial u_i}{\partial t} = \frac{u_i - u_{i-1}}{dx} \tag{2.4}$$

2.2.3 ODE solver

The numerical method utilised for this study was ode15s in Matlab R2011 b. This is a solver designed to solve differential algebraic equations (DAEs), a good description of the system of equations to be solved. ODE 15s is better for stiff systems (Shampine et al., 2003), while ODE 45 is better for non stiff systems. A stiff system is defined as one in which certain numerical methods are unstable, that is they either move about or away from the solution.

To find which solver would be best, the model was run using both algorithms. The time for each integration step was recorded, along with the number of calls to the systems of DAEs. This was performed at different felt movement rates, equivalent to different integration times. At each movement rate the integration tolerance was also varied. This factor is described in the next paragraph. All tests were also conducted with the use of sparsity and without. Table 2.1 shows the variables tested. Five integration steps were performed at each configuration, the results of which are shown in tables 4.1, and 4.2. This is discussed further in section 4.2, which demonstrates that ODE 15s is the clear winner.

The ODE solvers used are numerical methods, that is they take a step towards the solution rather than solve the equations algebraically. The process requires an exit criteria at which the solver has reached the solution of the given set of variables. This is achieved by looking at the 2–norm of the relative change in the output variable matrix compared to that of the previous iteration. The solver will keep iterating and hence getting closer to the actual solution until this has reduced to an acceptable limit, this is shown in equation 2.5, where x is the results matrix. By default this limit is set to 1×10^{-6}, which is normally acceptable. However very stiff systems may require a decreased tolerance, while some systems the tolerance may be reduced with little accuracy loss.

$$\text{tolerance} = \left\| \frac{x_i - x_{i-1}}{x_i} \right\|_2 \tag{2.5}$$

The 2–norm of a vector can be defined as in equation 2.6, which is then a method by which the size of a difference matrix can be analysed.

$$\|x\|_2 = \sqrt{x_1^2 + x_2^2 + x_3^2 ... + x_{n-2}^2 + x_{n-1}^2 + x_n^2} \tag{2.6}$$

Rate \ Tol	1×10^{-6}	1×10^{-5}	1×10^{-4}	1×10^{-3}	1×10^{-2}	1×10^{-1}	1
0.1	✓	✓	✓	✓	✓	✓	✓
1	✓	✓	✓	✓	✓	✓	✓
5	✓	✓	✓	✓	✓	✓	✓
10	✓	✓	✓	✓	✓	✓	✓
100	✓	✓	✓	✓	✓	✓	✓

Table 2.1: ODE speed test variable matrix

2.2.4 Jacobian Matrix

The accuracy of the model was linked to the number of segments used in the method of lines. Then number of equations to be solved is proportional to the square of the number of segments, as the method utilised a Jacobian matrix. Hence any increase in segment number results in a large increase in integration time. As the number of equations that needs to be solved is proportional to the number of segments, a method of informing the solver which equations are non–zero is required. This was achieved by passing into the solver a sparse matrix, the non–zero elements of which corresponded to the elements of the Jacobian matrix to be solved.

The Jacobian can be of two forms, banded or not. A banded Jacobian matrix is one in which all of the non–zero elements are found along the diagonal. If this is the case then a banded solver can be used, “since it would know in advance where the non–zero elements occur, and it would therefore not have to search for the non–zero elements and follow the resulting logic to use these non–zero elements” (Schiesser and Griffiths, 2009), for example ODE 45. The ability to use non–zero elements not on the diagonal adds complexity to a sparse solver. However for a stiff system this increased complexity is greatly compensated for improved ability to arrive at a solution.

For the system as described in section 2.4, the general form of the Jacobian matrix is given as equation 2.7. The form used in this study showing which elements are non-zero is given by

equation 2.8, where m is the total number of segments used in the model. It is evident that this is not a bounded form of the Jacobian, reinforcing the use of ODE 15s over ODE 45. A bounded Jacobian is one in which all the non–zero elements are about the diagonal, ODE 45 is optimised to solve systems of this form, while ODE 15s works well on non–bounded systems. The general pattern in equation 2.8 is that of the diagonal and the values directly adjacent, also including those m across.

$$\mathrm{J} = \begin{vmatrix} \frac{\partial U_1}{\partial x_1} & \frac{\partial U_1}{\partial x_2} & \cdots & \frac{\partial U_1}{\partial x_n} \\ \frac{\partial U_2}{\partial x_1} & \frac{\partial U_2}{\partial x_2} & \cdots & \frac{\partial U_2}{\partial x_n} \\ \vdots & \vdots & \ddots & \vdots \\ \frac{\partial U_n}{\partial x_1} & \frac{\partial U_n}{\partial x_2} & \cdots & \frac{\partial U_n}{\partial x_n} \end{vmatrix} \tag{2.7}$$

$$\mathrm{J} = \begin{array}{c|ccccccccc} {}_{j}\backslash^{i} & 1 & 2 & 3 & 4 & 5 & \ldots & m_i & m_{i+1} & m_{i+2} \\ \hline 1 & 1 & 1 & 0 & 0 & 0 & \ldots & 1 & 0 & 0 \\ 2 & 1 & 1 & 1 & 0 & 0 & \ldots & 0 & 1 & 0 \\ 3 & 0 & 1 & 1 & 1 & 0 & \ldots & 0 & 0 & 1 \\ 4 & 0 & 0 & 1 & 1 & 1 & \ldots & 0 & 0 & 0 \\ 5 & 0 & 0 & 0 & 1 & 1 & \ldots & 0 & 0 & 0 \\ \vdots & \vdots & \vdots & \vdots & \vdots & \vdots & \ddots & \vdots & \vdots & \vdots \\ m_i & 1 & 0 & 0 & 0 & 0 & \ldots & 1 & 1 & 0 \\ m_{i+1} & 0 & 1 & 0 & 0 & 0 & \ldots & 1 & 1 & 1 \\ m_{i+2} & 0 & 0 & 1 & 0 & 0 & \ldots & 0 & 1 & 1 \end{array} \tag{2.8}$$

2.3 Heat transfer

2.3.1 Radiation

All bodies emit energy in the form of electromagnetic radiation. The level of radiation depends on the temperature of the body, and the wavelength measured. Pyrometry is a technique which analyses the intensity and wavelength in order to find the emittance temperature of a body.

Plank's law of radiation gives the relationship between radiation strength I, absolute temperature T, and wavelength λ as follows, (Yamazaki et al., 2009)

$$I = \varepsilon \frac{2C_a}{\lambda^5} \frac{1}{\exp\left(C_b/\lambda T - 1\right)} \tag{2.9}$$

ε, emissivity; $C_a = 5.9548 \times 10^{-17}\left(\mathrm{Wm}^2\right)$; $C_b = 0.014388\,(\mathrm{mK})$

I is thus distributed in a single peak with respect to λ, where the shape and placing is dependent on T. The wavelength at which this peak occurs at a certain temperature is given by Wien's displacement law as follows

$$\lambda_m T = 2.8978 \times 10^{-3}\,(\mathrm{m\ K}) \tag{2.10}$$

A pyrometer measures intensity of emitted radiation at a given wavelength (Yamazaki et al., 2009). Hence by using the equation 2.10 it is possible to find the temperature of the body if the emissivity is known. For most bodies at close to standard conditions this will be close to 1, however this value can vary greatly with surface chemistry and temperature. Therefore for pyrometry of a high temperature body, for example carbon at 1000 °C+ another method is required.

If we make the assumption that the emissivity of a body does not change greatly over a narrow wavelength band then the temperature of an unknown body can be found. By measuring the wavelength and intensity at two different colours the temperature can be found as follows. First we combine the two equations at different temperatures,

$$\frac{I_1}{I_2} = \frac{\varepsilon_2}{\varepsilon_1} \left(\frac{\lambda_2}{\lambda_1}\right)^5 \frac{1 - \exp\left(C_b/\lambda_2 T\right)}{1 - \exp\left(C_b/\lambda_1 T\right)} \tag{2.11}$$

where subscripts 1 and 2 refer to wavelengths 1 and 2 respectively. As we will assume that the emissivity does not vary over the range of λ_1 to λ_2 (Wien's approximation) (Yamazaki et al., 2009) then:

$$\frac{I_1}{I_2} = \left(\frac{\lambda_2}{\lambda_1}\right)^5 \frac{\exp\left(C_b/\lambda_2 T\right)}{\exp\left(C_b/\lambda_1 T\right)} \tag{2.12}$$

Rearranging the above for temperature(our goal) we get the following,

$$T = \frac{C_b\left(\lambda_1 - \lambda_2\right)}{\lambda_1 \lambda_2} \frac{1}{\ln\left(I_1 \lambda_1^5 / I_2 \lambda_2^5\right)} \tag{2.13}$$

giving the temperature of a body of unknown emissivity as a function of the spectral intensity at two different wavelengths. These values were chosen as they fall in the range at which a carbon arc is relativity transparent. In this case the radiation of the arc plasma does not significantly affect the anode radiance observed.

2.3.2 Natural Convection

Natural convection is the process by which a gas moves due to a thermal gradient. This thermal gradient creates a density gradient, which causes the low density gas to rise due to buoyancy forces on it. This is shown in equation 2.14, where F is the vertical force, g is acceleration due to gravity, V is the volume of the object or gas bubble, and ρ is the difference in densities of V and the surrounding fluid.

$$F = \rho g V \tag{2.14}$$

where
F = the vertical force, [N]
g = acceleration due to gravity, [m.s^{-2}]
V = the volume of the object or gas bubble, [m^3]
ρ = is the difference in densities of V and the surrounding fluid, [kg m^{-3}].

For fibrous insulation of sufficient density the unit cell of trapped air is sufficiently small to limit natural convection. The tendency of a fluid to natural convection can be characterised by the fluid buoyancy number, the Rayleigh number. This has been modified (Bhattacharyya, 1980) for fibrous insulations as in equation 2.15; where for a Rayleigh number of less than 40, natural convection can be ignored when modelling heat transfer. Some authors give this limit as low as 13.4 (Joshi and Sukhatme, 1973). For the felt geometry and thermal profile used in this work the Rayleigh number is about three orders of magnitude below either limit. Hence natural convection was ignored in this work.

$$\mathrm{Ra} = g\frac{\beta\rho^2 C_p}{\mu} \times \frac{\mathrm{K}}{k} \times \Delta T \times \mathrm{D} \tag{2.15}$$

where

β = coefficient of volume expansion of air,[K^{-1}]
ρ = mass density of air, [kg m^{-3}]
C_p = specific heat of air, [J kg^{-1} K^{-1}]
K = permeability of the solid skeleton, [m^2]
ΔT = temperature difference between hot and cold faces, [K]
D = distance between the hot and cold faces, [m]
μ = dynamic viscosity of air, [Pa s]
k = apparent thermal conductivity of the porous medium without any motion of interstitial fluid, [W m^{-1} K^{-1}]

For vertical insulation this rule of thumb changes and is dependent on the vertical area. This changes to a ratio of $Ra/A < 4$, where A is given by equation 2.16. This will equate to a situation in which natural convection is negligible.

$$A = \frac{L}{D} \tag{2.16}$$

where L is the vertical height, and D is the distance through the insulation from the hot to the cold face.

2.3.3 Joule heating

ANSI/IEEE Standard 100–1988 defines the Joule effect as, the evolution of thermal energy produced by an electric current in a conductor as a consequence of the electric resistance of the conductor. (Erickson, 1995)

This defines all types of resistive heating as joule heating. The power released due to resistance by an electric current is given by equation 2.17

$$\frac{\partial E}{\partial t} = W = R \times I^2 = R \times \left(\frac{V}{Z_c}\right)^2 \tag{2.17}$$

where
W = power released, [W]
R = the resistance to current flow, [Ω]
I = current, [A]
V = voltage applied across the conductor, [V]
Z_c = the total impedance to current flow, [Ω]

In the arc reactor used in this study this effect heated the carbon felt anode. The electric pathway is shown in figure 2.1, where red represents current flow. Electrons from the arc enter the carbon felt, and then pass through this travelling to the water cooled Titanium anode support. To get an understanding of the size of this heating, equation 2.17 is used, where the resistance is found using the resistivity of the felt via equation 2.18. Z_c was found by direct measurement of the felt sample. This is described further in Appendix .2.

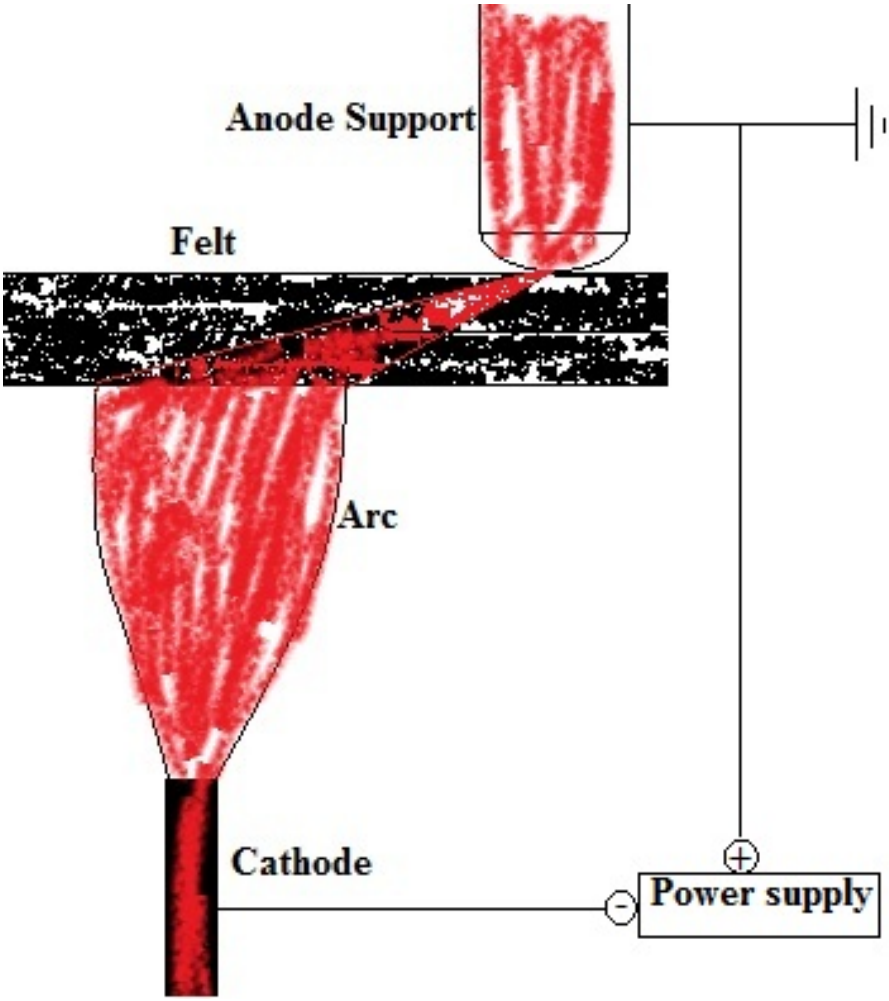

Figure 2.1: Arc electric pathway

$$R = \sigma \frac{L}{A} \tag{2.18}$$

where

R = the resistance to current flow, [Ω]
σ = resistivity, [Ω mm]
L = length of electrical pathway, [mm]
A = cross-sectional area of current pathway, [mm^2]

For SGL carbon fibre felt at 2.7 mm thick the resistance is, R=3 Ωmm $\times \frac{10\text{mm}}{3\text{mm}\times 20\text{mm}} = 0.83\Omega$ equivalent to a joule heating effect of $W = 0.83\Omega \times 14A^2 = 163W$. For the geometry of this electrical pathway see figure 2.1. The power supplied by the power supply is P = I $\times$ V =14 A $\times$ 45 V = 630 W, therefore this is a significant portion of the total.

2.4 Felt model

The model used in this study is based on that developed by Stark and Fricke (Stark and Fricke, 1993), which was based on the work of Bhattacharyya (Bhattacharyya, 1980). This model was developed to understand heat transfer through porous fibrous insulations, of which carbon fibre is a good example. The model is outlined in the following pages.

The heat transfer through a fibrous insulation is not simply a combination of the solid and gaseous components. If these are combined linearly this will typically underestimate the total thermal conductivity λ_{sg} (Stark and Fricke, 1993), for composites of density ρ of greater than about 5 kg m^{-3}. At densities of 300 kg m^{-3} this error is of the order of 20%. The carbon felt used in this study has a density of 180 g m^{-2} = 67 kg m^{-3}. Hence this linear approach would not be correct. This approach will be first discussed in the development of a more correct model.

The heat flux through a fibrous insulation can be simplified as the sum of conduction and radiation. The conduction portion is composed of two components, solid phase, and gas phase. The conduction through the solid phase is the combination of conduction through each fibre, and from fibre to fibre. For the carbon felts used in this study natural convection can be ignored, due to the small spacing between fibres which effectively traps the air, explained in section 2.3.2. This summation is given in equation 2.19

$$q_{\text{total}} = q_{\text{sg}} + q_{\text{r}} \tag{2.19}$$

where the subscript sg denotes the combined conduction through the gas phase, solid phase, and solid couplings; while r represents the radiative component. Utilising Fourier's empirical law (equation 2.20) and the assumption that ΔT is the same for all heat transfer components,

equation 2.19 transforms to equation 2.21. The previous assumption is valid over small regions; these will be used via the modelling process of method of lines which divides the felt into small segments for integration, discussed in section 2.2.2 on page 16.

$$q = -\lambda \Delta T \tag{2.20}$$

$$\lambda_{\text{total}} = \lambda_{\text{sg}} + \lambda_{\text{r}} \tag{2.21}$$

Here Stark starts with a basic model, and then further develops the model adding further levels of complexity increasing the accuracy of the approximation. The most accurate of the three models developed by Stark and Fricke is that which was used in this work. The basic model and modified basic model are hence stepping stones to that final model.

2.4.1 Basic model

In the basic model fibres with any orientation can be used. However the following assumptions are made by Bhattacharyya (1980)

1. The fibrous insulation can be approximated as a homogeneous medium of thermal conductivity λ_{sg}
2. Interactions between fibres influencing λ_{sg} can be averaged over a unit volume
3. Any individual fibre can be assumed to be a spheroid whose major axis is very large compared with the minor axis

The first assumption is valid due to the felting process. Carding and then the creation of the batt create a uniform material. The needling process is also uniform, with constant frequency of needling and rate of textile movement. The PAN fibres used are of uniform size with size distribution as discussed in section 4.1. The same argument can be used to validate assumption two.

Assumption three is also valid due the the fibre geometry. With an average diameter of 9 μm and length of about 6 mm, this ratio is of the order of 500:1. SEM images in figure 1.9 show the cylindrical shape of the fibres.

The orientation of the fibres in the insulation is described by the parameter Z, which represents the fraction of the fibres orientated perpendicularly to the macroscopic heat flow. Bhattacharyya

gives values of Z = 1 for fibres perpendicular to heat flow, through to Z = 0.66 for randomly orientated fibres (Bhattacharyya, 1980). This parameter is typically fitted by the method of least squares (Shuyan et al., 2009), see Section 4.1 and figure 4.1.

The thermal conductivity through the composite system is found by modifying the model developed by (Fricke, 1924). The model outlined by Fricke was developed to describe the electrical conductivity through biological suspensions such as blood. This general model was modified for spheroids in a gaseous medium. Fricke's model is outlined in appendix .3 on page 78. This approach for electrical conductivity can be used for thermal conductivity Bhattacharyya (1980). The form used is given in equation 2.22. However this basic model still tends to underestimate the actual heat transfer (Stark and Fricke, 1993) as fibre orientation is ignored.

$$\lambda_{\mathrm{sg}}^{\mathrm{BM}} = \lambda_0 \left(1 + \frac{Cr - 1}{1 + Vr\left(1 + Z^{(Cr-1)/(Cr+1)}\right)} \right) \tag{2.22}$$

2.4.2 Modified model

As the basic model ignores the contacts between fibres Stark made further improvements (Stark and Fricke, 1993). Each contact is in effect a thermal resistance to heat transfer, and this can be represented by an electrical analogy as in figure 2.2.

The following assumptions are made

1. The unit cell height is now $(m+1) \times 2r$, compared to $m \times 2r$ in the basic model, see figure 2.3
2. The fibre to fibre contact area is A_{ct}
3. The effective area of the gas volume acting as a parallel resistance R_s is $o \times A_{ct}$

Where "m" is the height of the unit cell in multiples of fibre diameter. While "o" is the area of the unit cell over which fibres are not contacting, the area over which conduction through the gas phase occurs.

The contact resistance R_{ct} is calculated as developed by Kagner (Kaganer, 1969), using the contact radius of Hertz (Hertz, 1882) for elastic deformations of cylinders with $a_{ct} \ll r$ (Fricke, 1924)

with the a contact resistance of

$$R_{\mathrm{ct}} = {}^{1}/_{(2a_{\mathrm{ct}}\lambda_{\mathrm{sol}})} \tag{2.23}$$

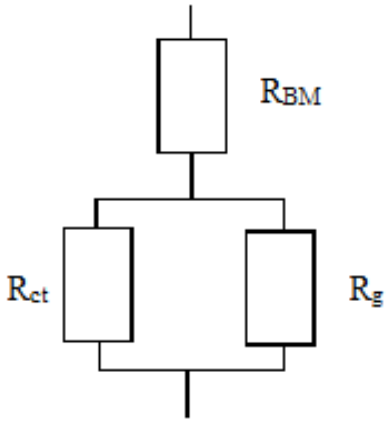

Figure 2.2: Electrical circuit diagram analogy of improvements of the modified model over the basic model (Stark and Fricke, 1993)

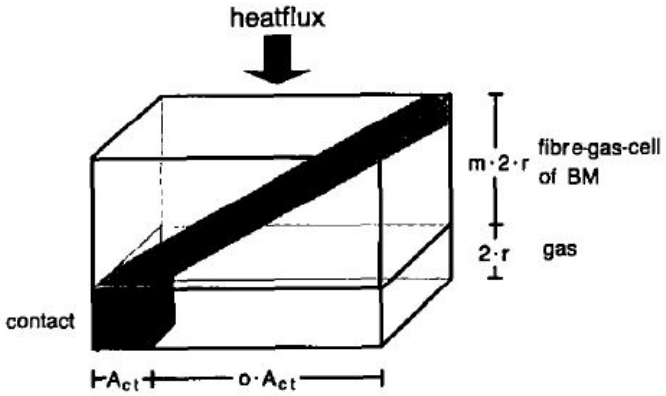

FIG. 2. Cell of the modified model.

Figure 2.3: Unit cell of model(Stark and Fricke, 1993)

with a cell area of $S_{cell} = (o+1)\,A_{ct}$ giving the total thermal conductivity of the solid for this improved model of

$$\lambda_{ss}^{MM} = \frac{(m+1)\cdot 2r}{S_{cell}\left(R_{BM} + \left(\frac{1}{R_g} + \frac{1}{R_{ct}}\right)^{-1}\right)} \tag{2.24}$$

The orientation of the fibres in the unit cell can be calculated from one of the two probability functions as below(Stark and Fricke, 1993). Where ϑ is the angle of a fibre in the unit cell.

$$h(\vartheta) = \begin{cases} \kappa & \vartheta < \Theta \\ \xi \cdot \kappa & \vartheta \geq \Theta \end{cases} \qquad \xi = \frac{1}{2/z - 2} \tag{2.25}$$

$\xi = 1$ for randomly orientated fibres, for a continuous form

$$h(\vartheta) = \begin{cases} \beta \cdot \vartheta & \vartheta < \Theta \\ (\beta \cdot \Theta - y \cdot \Theta) & \vartheta \geq \Theta \end{cases} \tag{2.26}$$

with $\beta > 0$

$$\frac{\beta}{y} = \frac{(1-\mathrm{Z}) \cdot (1 - \sin(\Theta))}{\mathrm{Z} \cdot \sin(\Theta) - \Theta \cdot \cos(\Theta)} \tag{2.27}$$

In the case that all the fibres are orientated perpendicular to the macroscopic heat flow, ie $\beta \gg y$ this function simplifies to a good approximation (Stark and Fricke, 1993).

Stark then uses these functions to find the fraction of fibres which are perpendicular to the macroscopic heat flow, as below

$$Z = \frac{\int_0^{90} \int_{\Theta}^{90} h(\vartheta)\, l^2 \sin\vartheta \, d\vartheta \, d\varphi}{\int_0^{90} \int_0^{90} h(\vartheta)\, l^2 \sin\vartheta \, d\vartheta \, d\varphi} \tag{2.28}$$

were Θ is the angle about which fibres are considered either parallel or perpendicular to the macroscopic heat flow. Knowing that for randomly orientated fibres the probability function is constant, and that $\mathrm{Z} = 0.66$, the angle Θ used in both probability functions can be derived from equation 2.28 as

$$\cos\Theta = 2/3, \Theta = \arccos 2/3 \tag{2.29}$$

m and o are given as a function of the fibre orientation, as orientation this will change the size of the unit cell.

$$m + 1 = \frac{1}{2}\frac{l}{r}\cos\phi_0 \tag{2.30}$$

$$o + 1 = \left(\frac{l}{r}\right)^{2/3} \frac{(0.5\sin\vartheta_0)^{s\frac{1}{3}}}{\pi\left(1.5\left(1-\mu_0^2\right)^{P_{exi}/Y_0}\right)^{2/3}} \tag{2.31}$$

$$\frac{l}{r} = \left(\frac{\pi\rho_0/\rho}{0.5\sin^2\vartheta_0\cos\vartheta_0}\right)^{1/2} \tag{2.32}$$

2.4.3 Modified model with connection parameter

In section 2.4.1 we ignored the contacts between fibres, and in section 2.4.2 we included the effect of contacts between fibres. However by the method used, with one unit cell it was assumed

that all adjacent fibres were in direct contact with each-other. This is not the case, and we will now subdivide the unit cell utilised to get equation 2.24 into eight sub cells.

The heat flux through the unit cell can be found by looking at that through the centre of the cell, the point at which a corner of each cell is in contact. The direction of the fibres in each sub cell can be chosen to orientate in one of four different directions, giving 4^8 total possible orientations. The heat flux can then be given as between the limits of maximal or minimal numbers of fibres parallel to the macroscopic heat flow. These two limiting cases given values of 0.6836 and 0.5384, the mean of these two values will be used.

The combined heat flux is then given by equation 2.33 as, where $\lambda_{\mathrm{sg}}^{\mathrm{BM}}$ is given by equation 2.24.

$$\lambda_{sg}^{\mathrm{MMC}} = (m+1)\left\{\frac{m}{\lambda_{sg}^{BM}} + \frac{o+1}{o}\frac{1}{\lambda_g + \frac{4\lambda_0 Ar}{o\pi a_{ct}}}\right\}^{-1} \tag{2.33}$$

2.5 Graphitisation

Many intensive studies on *stabilisation* of PAN were done in 1950s and 60s, and the modern understanding of PAN graphitisation is based on this work. This has lead to the accepted reaction pathway as that of nitrile groups undergoing a cyclisation reaction. However this has not been experimentally proven. This understanding is via circumstantial evidence.

The reaction pathway can not be deduced from IR spectroscopy, with different authors giving conflicting interpretation of the same spectra. As PAN is insoluble after thermal stabilisation it is not possible to detect changes using nuclear magnetic resonance, as the peaks observed are very wide. This means that the NMR spectra could represent any one of multiple structures or combinations of. The reaction is exothermic suggesting a concerted reaction, but this is also inconclusive as nitrile polymerisation can also be exothermic (Rahaman et al., 2007).

PAN $[C_3H_3N]_n$ gives a high carbon yield, is thermally stable, and has an extremely oriented molecular structure when subjected to low temperature treatment(200–400°C (Rahaman et al., 2007; Fitzer and Weisenburger, 1976)).

The graphitisation of PAN proceeds via the following steps;

1. Precursor PAN fiber
2. Stabilisation–oxidation in air
3. Carbonisation–Heat treatment in nitrogen

4. Graphitisation–Heat treatment in argon

Stabilisation is an essential time consuming step before carbonisation and/or graphitisation. In this stage the PAN fibres are heated to moderate temperatures, usually at 180–300 °Cat rates of about 1–5 °C min $_{-1}$ (Mittal et al., 1997), Fitzer and Weisenburger found that 270 °C was required while Mittal et al. gave 400 °C. Higher stabilisation temperatures have been linked with a slightly increased density of 1.52 compared to 1.45 g cc^{-1}, along with lower hydrogen ratios. This causes thermal stability due to the creation of a ladder structure, a process called cyclisation. This produces a visual change in the PAN fibre, from an initial white, through to shades of yellow and browns to the final stabilised black colour. The mechanism behind this colour change has not been explained to date (Rahaman et al., 2007). This thermal stability results in fibres which can no longer melt. However if this stage occurs at too high a temperature, melting can occur before stabilisation resulting in fused fibres.

High temperatures can also burn the fibres, as this stage normally occurs under atmospheric oxygen concentrations, unlike the nitrogen environment used during carbonisation. Figure 2.5 shows the reaction pathway of the cyclisation reaction. This starts with the polymer structure of PAN, which is then converted to the ring structure of stabilised PAN. The kinetics of this stage are of little interest to this work, so will not be explored in detail. Other reactions that occur during this stage include those of dehydrogenation, aromatisation, oxidation. However these are not considered of much importance to the general structure of the stabilised PAN.

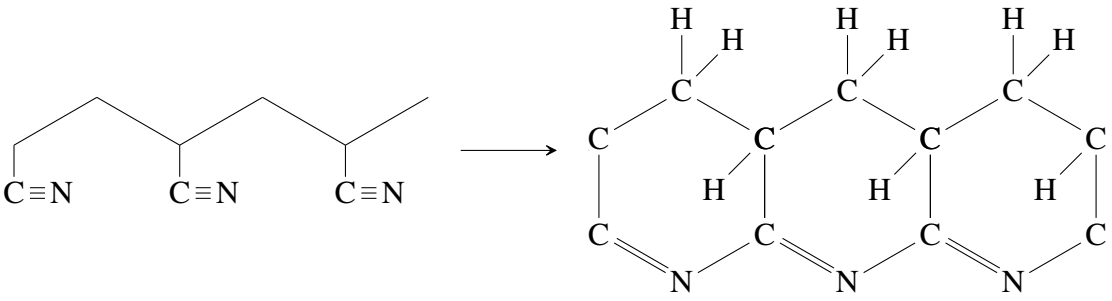

Figure 2.4: Cyclisation reaction of PAN

Carbonisation is a process by which the stabilised PAN structure is converted to a high carbon form. This involves the removal of some of the remaining nitrogen, oxygen, and hydrogen. To achieve this the PAN fibres are heated to temperatures of 600–800 °Cfor 2–5 hours (Sonobe et al., 1988). Stretching of the fibres during this pyrolysis process helps develop high tensile modulus and improves the fibre strength (Perepelkin, 2002).

The final process that can occur is that of graphitisation. This is a high temperature process which converts the carbon polymer structure to a graphite structure. This is thought to be an

important aspect of this work, as a graphitised structure has a higher electrical conductivity than that of carbon. The kinetics of the stage are explained further in section 2.5.1 below.

2.5.1 Kinetics

Graphitisation follows an Arrhenius rate law with a single pre–exponential factor see equation 2.34 Fitzer and Weisenburger (1976); Greene et al. (2002). k is the reaction rate constant, k_0 is the pre–exponential factor, E_a is the activation energy, R is the universal gas constant and T is the reactor temperature.

$$k = k_0 e^{\left(\frac{-E_a}{RT}\right)} \tag{2.34}$$

The activation energy is 260 $\frac{\text{kcal}}{\text{mol}}$ Fitzer and Weisenburger (1976). The pre–exponential factor is not given by any author, so this was found by a least squares regression from the published work. Fitzer and Weisenburger gives a plot of the contraction of the basal spacing of the graphite layers at different temperatures against the log of time. This data was collated from four different authors. The code used to predict the degree of graphitisation over time at a set temperature is given in Appendix .1.1 on page 69.

A fit of the predicted graphitisation at the same temperatures given by Fitzer and Weisenburger was produced over the same temperature range. This was a problem with one degree of freedom, hence the pre–exponential factor was adjusted to get the best fit between the two sets of data. This was found to 1.2×10^{19} s^{-1}, give the reactor rate as in equation 2.35, for a single order Arrhenius equation as per equation 2.34.

$$k = 1.2 \times 10^{19} e^{\left(\frac{-1.16\times10^6}{8.314\times T}\right)} \tag{2.35}$$

2.6 Vaporisation kinetics

It was thought that the vaporisation and re–deposition of carbon was important. As the change in degree of graphitisation was found to be low (see section **??** in the results), the next likely hypothesis for the improved effect observed with arc treated fabric was the change in surface chemistry. This may occur through the vaporisation and deposition of carbon forms, hence it was of interest to predict the rate at which this could occur.

A paper written by Abrahamson et al. in 1980 outlined a mechanism by which the erosion of carbon under a arc occurs (Abrahamson et al., 1980). A figure was given showing the linear relationship between the logarithm of the erosion rate and the inverse of temperature; this was fitted over seven orders of magnitude of erosion rate from 2500–4500 K. By picking two points on the linearly fitted line this relationship could be found, this is given in equation 2.36.

$$r = k_0 e^{\left(\frac{-E_A}{RT}\right)} \tag{2.36}$$

were

r = erosion rate [kg m^{-2} s^{-1}]

k_0 = rate constant = 5.8×10^{12} [kg m^{-2} s^{-1}]

E_A = activation energy = 9.0×10^5 [J mol^{-1}]

R = universal gas constant = 8.314 [J mol^{-1} K^{-1}]

T = temperature of erosion [K]

Using the fitted Arrhenius relationship and the predicted thermal profile (via the model outlined in section 2.4.3), the vaporisation of the carbon felt was predicted. The results are given in section **??**, with the code in Appendix .1.6, which replaced the code for graphitisation. Compare this activation energy to that of graphitisation, 9.0×10^5 J mol^{-1} for vaporisation to 1.1×10^6 J mol^{-1} for graphitisation.

Chapter 3

Arc Reactor design and development

The arc reactor used in this investigation was a modified version of that developed over many year by multiple collaborators, all based in the Chemical Engineering department under Adjunct Professor John Abrahamson. The initial design was an attempt to replicate the work of Abrahamson and Wiles in 1978 (Wiles and Abrahamson, 1978). During this work T.E.M, and S.E.M imaging was used to look at the surfaces of carbon anodes after operation at 11 A in N_2 and air. This resulted in figure 3.1 which shows carbon nano–tubes, many years before the traditionally accepted date of discovery in 1991.

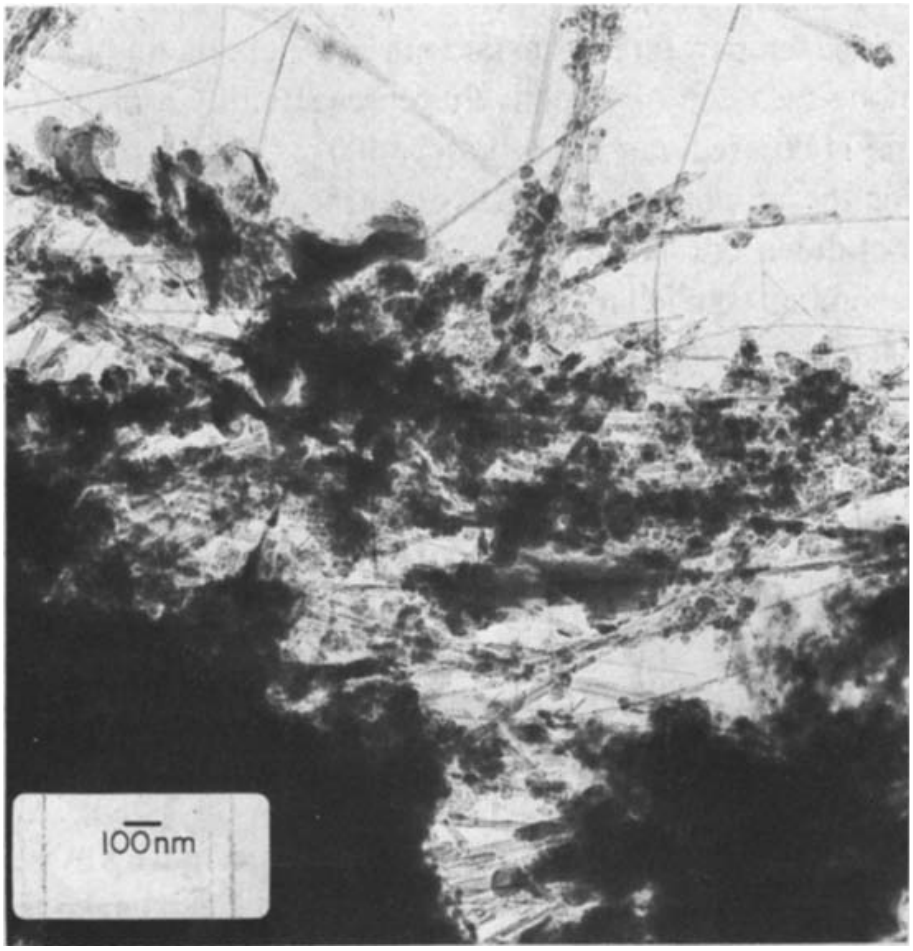

Figure 3.1: T.E.M image of carbon anode after discharge at 11 A (Wiles and Abrahamson, 1978)

3.1 Previous Work

A project to reproduce these results was initiated in 1999. Two final year students were given the task of designing and then operating a arc reactor based on the 1978 design, but continuously fed with carbon fabric. The two students Hill and Mani, designed a continuous version of the reactor which was then used by multiple postgraduate students in their studies. This reactor was also used in batch mode.

An issue encountered by all previous collaborators was the stability of the arc. This was thought to be linked to either one of the following or a combination of, the power supply used, the arc gap, arc geometry, the fabric movement speed or the cathode diameter. It was found during the present study in 2014 that the dominant factor was the thermal conductivity of the cathode material. This is explained further in section 3.5.

3.1.1 1975 Batch Reactor

The batch reactor consisted of a brass cylinder capped at both ends with brass plates. Into this extended two carbon rods perpendicular to each–other. Both of these could be manually moved via friction rollers placed external to the chamber. There were water cooled copper coils between the friction rollers and the arc chamber. The carbon rods entered the arc chamber through holes lined with boron nitride, which is an electrical insulator stable at the high temperatures present close to the arc discharge.

The arc atmosphere was controlled via a gas feed. The construction of the reactor was such that the arc chamber pressure was about atmospheric. The composition of the gas feed was able to be controlled from full nitrogen, to a nitrogen air mixture through to full air.

Viewing ports were positioned in the sides of the chamber. An image of the arc was then projected from these through a lens. This was then focused onto a screen at a magnification of four times. The result of which was the ability to control the arc gap to within 0.25 mm of the desired value. The gauge which was used to control arc gap is shown in figure 3.2, where each increment is 1 mm absolute or 0.25 mm at the arc. The bright oval in the figure is the hot cathode tip, while the glow is the arc plasma, and the bright vertical line on the right is the surface of the felt. The carbon rods used were spectroscopic grade, Carbon L 113 SP with diameters of 6.05 mm and 3 mm for the anode and cathode respectively.

The design was unsuccessful (bin Mohamed Yusoff, 2008) in reproducing the fibres as in figure 3.1. Further modifications were then carried out by Can Ulubay in 2002, however carbon nano-fibres were still unable to be produced. Further efforts were then focused on the continued development of the continuous arc reactor as described in the section 3.1.2.

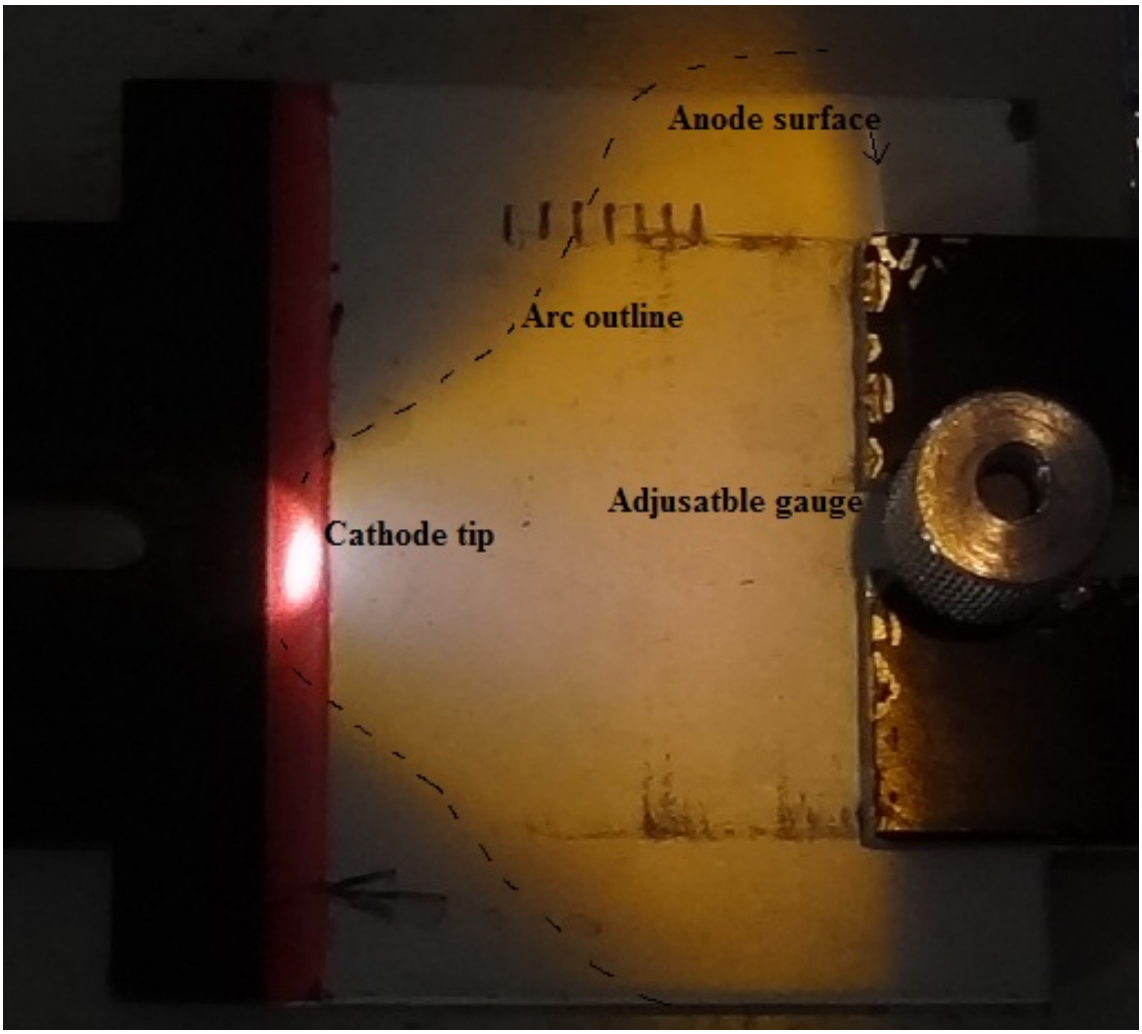

Figure 3.2: Scale to control arc gap, VI reactor

3.1.2 2000's Continuous Arc Reactor

As a batch process is undesirable in a manufacturing process Professor Abrahamson instigated the development of a continuous arc reactor. This was initiated in 2000 with a final year student, Chan. The design of this was similar in method to the batch reactor described above in section 3.1.1.

The chamber of the reactor was a brass cylinder, with brass plates at each end, creating a sealed chamber. The anode and cathode were again perpendicular to each–other, housed in water cooled boxes enabling the position to be adjusted. The position could be adjusted in two dimensions; horizontally changing the arc gap, and vertically adjusting the position of the cathode relative to the anode support. The reactor was orientated so that the fabric anode moved vertically past a horizontal arc.

Viewing ports enabled the light from the arc to escape the chamber. This was then focused onto a screen via a lens, giving an image of the arc at four times magnification. This was then used to position the carbon rods to a desired distance, by the same method as used in the batch reactor. See figure 3.3 below sourced from (bin Mohamed Yusoff, 2008).

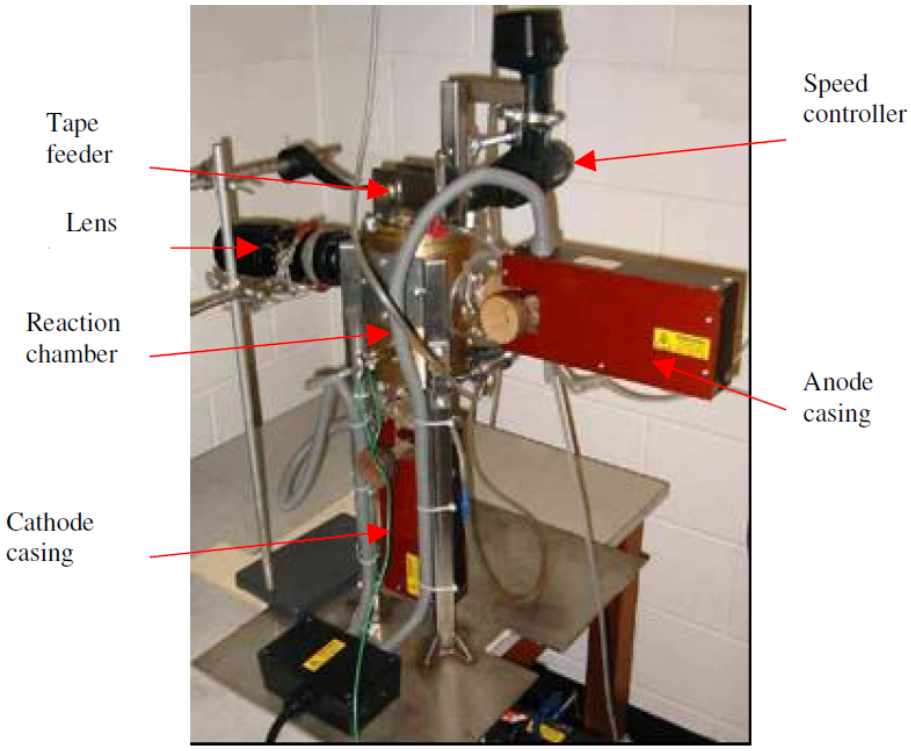

Figure 3.3: Continious Arc Reactor Version 1 (bin Mohamed Yusoff, 2008)

The continuous aspect of the reactor was that the anode is actually a moving material, a carbonised PAN fabric. This fabric entered the reactor chamber through a slot in the side, and was then pulled vertically through the chamber via the speed controlled motor from above. The arc then travelled from the vertical carbon cathode to the vertical carbon fabric, and then into the horizontal carbon anode support. The vertical face of the anode support was held against the carbon fabric, the tension of which provided adequate electrical contact.

There were two gas lines into the arc chamber, one below the arc and another above. Both of which were 99.9% oxygen free nitrogen, supplied by BOC. The gas feeds helped keep the chamber at the desired atmosphere.

Nanotubes were produced by Uluaby, similar in appearance to those found in the 1978 study (bin Mohamed Yusoff, 2008). Conditions for production were fabric movement speed below 2.1 mm s^{-1}, but atmosphere composition and arc gap were not given.

3.2 Oxygen Concentration

During the design and construction of the continuous arc reactor effort had been made to control the atmosphere of the arc chamber, as this is a important factor (Abrahamson et al., 1980; bin Mohamed Yusoff, 2008; Davies and Abrahamson, 1983). In the 1978 study it was found that a atmosphere composed of air either stopped the production of nano-tubes, or removed them after the local arc atmosphere is extinguished. As nano-tubes were desired a nitrogen chamber atmosphere was desired.

To achieve this, nitrogen was introduced into the arc chamber as described in section 3.1.2. The entrance and exit slots of the reactor chamber were of dimensions of 88×6 mm, with a nitrogen feed rate of 10 L min^{-1}, and a flow of 0–1.6 L min^{-1} through the porous anode support (bin Mohamed Yusoff, 2008). However due to the the production of carbon monoxide in the arc chamber gas extraction was a safety requirement. This was in the form of a gas hood above the apparatus, not shown in figure 3.3. The air velocity about the reactor when under the hood was recorded at between 4.0 and 7.5 m s^{-1}, depending on which hood was used.

As such the gas concentrations inside the reactor have been assumed to match those supplied via the feed tubes. However due to the extraction hood above the reactor this was not the case. The velocity of the extraction hood was measured to be a minimum of 4 m s^{-1}. This corresponded to a gas flow through the reactor of

$$A_{exitslot} \times V_{air} = 6\text{mm} \times 88\text{mm} \times 4000\frac{\text{mm}}{\text{s}} \times 60\frac{\text{s}}{\text{min}} = 1.28 \times 10^8 \frac{\text{mm}^3}{\text{min}} = 127\frac{\text{L}}{\text{min}}$$

which is an order of magnitude greater than the flushing flow of 10 L min^{-1}. Hence steps were then taken to more efficiently seal the chamber, such that the local chamber atmosphere was that desired.

The reactor was then sealed to achieve a nitrogen environment as had been previously assumed. This was by the construction of carbon felt seals. These were made from 10 mm thick pieces of felt which were placed against the tape exiting and entering the reactor. This resulted in a slight positive pressure at flushing gas flows of 4–7 L min^{-1}.

3.3 Anode Support Development

Previous work had focused on the arc and the anode surface, as the present goal was the production of carbon nano-tubes (bin Mohamed Yusoff, 2008). However this investigation is concerned

with the carbon fabric as a whole, not just the surface chemistry but also the physical and structural changes that occur inside each fibre.

Therefore only the total arc current was of interest. Efforts had been made to stabilise this current, to reduce ripples caused during the AC/DC conversion, reducing it from the order of 10 A down to 0.3 A (bin Mohamed Yusoff, 2008). Once the current had passed through the arc it had been assumed that it then went into the anode support, then back to the power supply. To confirm this, two ammeters were installed in the circuit, one between the anode support and the power supply, the other on the earth line. It was found that a large portion of current $\simeq 1/3$, was travelling through the earth line.

This charge must have travelled through the carbon fabric and earthed on the entrance and exit slots of the reactor. This is expected to have then heated the fabric via Joule heating, resulting in different thermal profiles compared to that expected. This was regarded as undesirable. As the oxidation rate is proportional to the exponential of the temperature; maintaining high temperatures away from the arc was expected to be detrimental, as this would result in increased oxidation. Efforts were then taken to reduce the earth current allowing the fabric to cool faster.

The anode support was constructed from a rod of graphite, with a porous graphite insert to allow gas flown through its centre. The surface of this was sanded with $\simeq 200$ grit emery paper, to remove any low conductivity surface deposits, the thickness of which are of the order of about 5 μ m (Wiles and Abrahamson, 1978). Hence this support required replacement frequently, with process stoppages every $2-5$ minutes. This was an unacceptable solution for a manufacturing process. A permanent solution was therefore required. The anode support was required to be conductive, able to withstand the high temperatures of the arc, and the abrasive action of carbon fabric pulling past it.

The design arrived on was a thin walled water cooled copper bar. The copper bar has the good electrical properties desired. The copper was protected from direct contact with the arc as it was placed behind the fabric, and also offset from the arc. The temperature of the anode material was of the order of $500-1500$°C, which is greater than the melting point of copper at about 1000°C; hence rapid cooling was required. Thin walls were used to increase heat transfer away from the external face of the support, a large flow rate of water was used with velocities of the order of 50 m s^{-1}. The shape of a bar was chosen for two reasons, 1) the flat face would provide good contact with the arc substrate, and 2) this would result in ease of manufacture.

This water cooled copper anode support (wccas) was constructed to be adjustable in two dimensions, as the ideal location was unknown. Initially the support was offset to produce a deflection in the fabric of about 5°, which was similar to that for the graphite support. However the electri-

cal contact was found to be insufficient. The tension on the fabric could not be increased, as it was already at about 70% of the ultimate tensile strength. It was found that increasing the offset to about 7°with 50N of tension across 55 mm width of fabric was required for good electrical contact. The current travelling through the earth wire had then dropped from $\simeq 1/3$ to about $\simeq 1/20$ of the total current.

3.4 Arc stability

It has been found that a stable arc is highly desirable. An unstable arc is one in which the cathode hot spot moves with respect to the cathode rod. This movement is either of the form of a rotation at almost constant frequency, or apparent "sticking" where the hot spot maintains the same position on the cathode tip.

This periodic or erratic behaviour of the cathode spot induces corresponding movement of the arc as a whole, so that the arc attachment on the anode moves laterally in a periodic or erratic fashion as the anode material moves past. "Sticking" of the cathode spot thus corresponds to a constant deviation of the arc track on the moving anode material for a period of time (up to 5 s has been observed).

When the wandering/ rotating behaviour is observed non-uniform tracks are produced so that instead of the centre of the track being directly above the cathode, the edge of the arc track may be directly above the cathode or even past it. This causes great difficulty in producing tracks bordering on each other. The "sticking" behaviour can be greatly damaging, as the arc is in one position for an extended period of time and the resulting treatment damages the anode material. Sticking times of greater than about 0.5 s have been found to cause the material to be destroyed during pasting.

This gives two objective measures of arc stability, the frequency of arc rotation, and the duration of any sticking. A stable arc is one in which neither of these phenomena are observed. Moderately stable is one in which no sticking is observed, and rotation frequency is of the order of about 1/3 Hz or less.

In order to maintain an arc the surface of the cathode needs to be able to easily emit electrons and therefore has to be hot. The arc can originate from any point at which the cathode is hot enough, it will then propagate perpendicular to the surface at this point. This is due to the movement of a concentrated flow of electrons from the surface, that induces a magnetic field which then pumps the arc plasma directly away from the surface. The arc is often in constant lateral motion on

the cathode surface, but will stay in one place if there is a sufficient thermal gradient along the surface to keep it there. The arc attachment itself heats the cathode. If the material making up the cathode has a high thermal conductivity we have found that the arc movement is over a large area (and the arc track is “unstable” and conversely when the thermal conductivity is low the arc attachment is small (and the arc track is “stable”). In fact, the transition between stability and instability occurs over a narrow thermal conductivity as shown in the work described below. The other major property of the cathode material is electrical resistivity which must be sufficiently low to allow the arc current to flow. This property may thus be considered as a possible influence on stability. However, experiments done with a wide variety of carbon materials used as cathode materials (each material with its own thermal conductivity and resistivity) showed that there was no clear correlation of stability with resistivity, in contrast with the clear correlation shown with thermal conductivity, as shown in the figure 3.4. Both of these properties are expected to be related both to the structure of the hydrocarbon precursor to the carbon, and to the temperature of heat treatment. The resulting final structure influences both thermal conductivity and resistivity e.g. in figure 3.4 treatments at successively higher temperatures are expected to result in a progression of materials with lower resistivity and higher thermal conductivities, i.e. from right to left and higher on the chart.

With a vertical carbon cathode, the carbon erodes and oxidises from the heated surface so that a pointed tip is formed. The formation of the tip appears to result from evaporation from the shank combined with deposit on the tip. For materials of lower thermal conductivity the stable arc attachment is developed on the small radius of the tip and the arc is vertical. For materials above a limiting thermal conductivity the hot area expands and becomes overall cooler, resulting in no strongly preferred location for electron emission. Hence a cathode of low thermal conductivity is desirable, preferably with 25 W (m K)$^{-1}$ or less, as shown in the figure.

To reduce the effects of thermal conductivity rods of smaller diameter can be used. This may make the radial radiative heat loss dominate over the axial conduction; this should and did result in stable arcs at reduced diameter. A cathode with marginal conductivity (25 W.m-1.K-1) was unstable at 6.1 mm diameter, however at 3.0 mm diameter this produced a marginally stable arc. This heat balance has not shifted far enough with the high thermal conductivity rods. For two materials (one with thermal conductivity 50 and the other with 37 W (m K)$^{-1}$) both 6.1 mm and 3.0 mm electrodes were unstable.

The values of resistivity and thermal conductivity reported here were measured as in section 3.5 and .2

3.5 Cathode thermal conductivity

A fixed length (100 mm) of each material rod was cut off and flat surfaces turned on each end. Fine fibrous insulation (alumina felt) was wrapped around the cylindrical surface and the temperature at all points was allowed to equilibrate with the surrounding air at room temperature. A surface temperature probe (K type thermocouple) was pressed against one end and the other end was subsequently pressed squarely against a compact steel block of approximate dimensions 100 mm x 100 mm x 100 mm held at 376 °C. The temperature of the cool end of the rod was noted at increasing times (every 10 s) up to 120 s.

Each temperature history was fitted with an analytical solution of the problem of transient heat transfer in one dimension, between two planes, starting from a constant temperature throughout, then suddenly one plane held at a constant different temperature and the other with zero heat transfer (insulated, or the symmetry plane of a double region). This problem was appropriate for the experimental rig because radial heat losses were deemed to be negligible, making the heat transfer one-dimensional. This problem was solved for the temperature of the symmetry plane by (Carslaw and Jaeger, 1976)and in dimensionless form the solution for the dimensionless temperature v/V was as in equation 3.1

$$\frac{v}{V} = 1 - \frac{4}{\pi}\sum_{n=0}^{\inf}\left[\frac{(-1)^n}{2n+1} exp\left(-\frac{(2n+1)^2\pi^2 T}{4}\right)\right] \tag{3.1}$$

where temperatures relative to the starting environmental temperature are used.

v = temperature of the symmetry plane (here, cool end) at time t [K]

V = constant temperature of the other plane (here hot end) [K]

T = κ t / L2, dimensionless time

κ = k / (ρ c) , thermal diffusivity, [$m^2 s^{-1}$]

k = thermal conductivity, [W $(m\ K)^{-1}$]

ρ = density, [kg m^{-3}]

c = specific heat capacity, [J $(kg\ K)^{-1}$]

t = time after step change in hot end temperature, [s]

L = length between two planes (length of rod), [m]

Inserting the relevant properties of density and specific heat capacity and length into the equation, using 11 terms in the series sum, one can adjust the unknown thermal conductivity k until a fit between the experimental and theoretical temperature / time profile is obtained. Good fits were obtained for all of the materials except for the two highest thermal conductivity materials. These showed a lower temperature rise profile than could be fitted by the theory at temperatures

above 130 °C(no other materials reached this temperature in the maximum time of 120 s). This discrepancy was thought to be due to a radial loss of energy to the insulation because of an evaporation of absorbed moisture from the insulation when the rod reached significantly above 100 °C.

In these two cases, the fit was confined to the early history for temperature v <130 °C. In these two cases, the thermal conductivity was corrected upwards, from 43 to 50 and from 45 to 60 $W.m^{-1}.K^{-1}$.

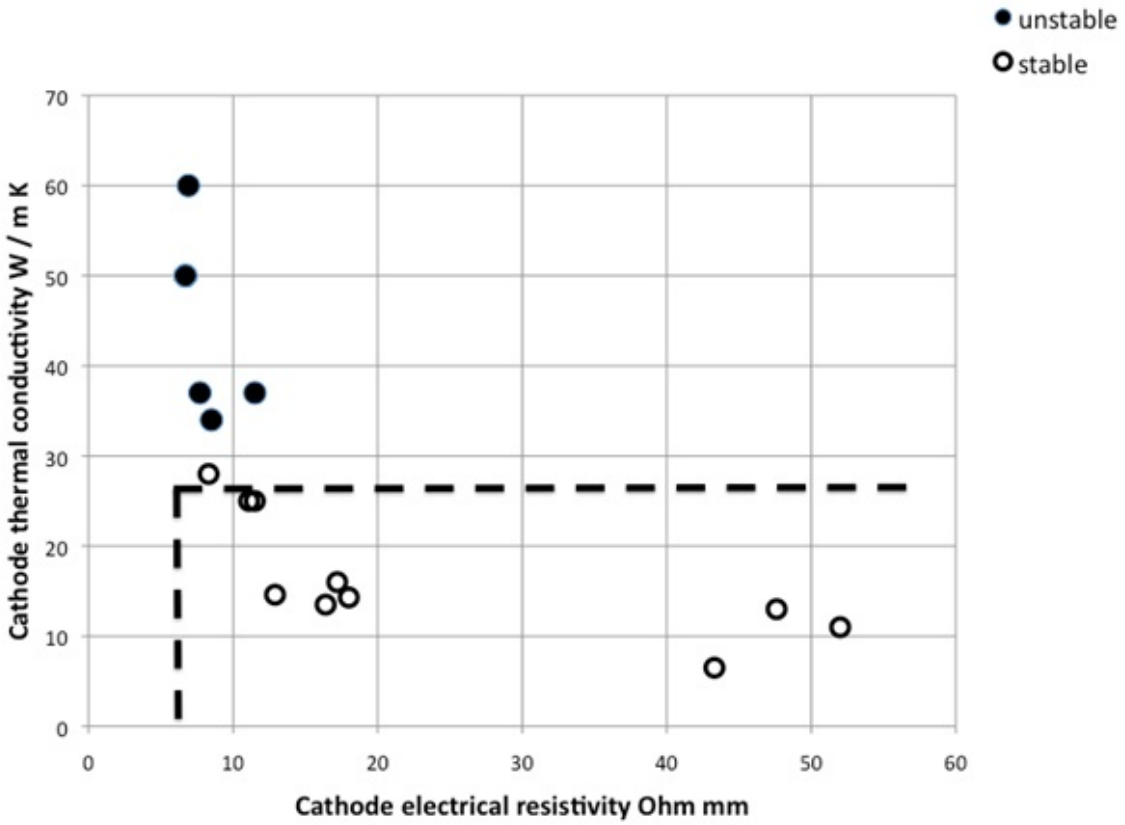

Figure 3.4: Thermal conductivity vs electrical resistivity for carbon rods

3.6 VII Arc Reactor

The arc reactor was able to ”arc treat“ only a single track at a time; this would have resulted in very slow process times if scaled up to the size of a full scale battery. As each track was 10-25 mm wide depending on arc parameters this would have required many passes through the arc reactor to treat the required full scale width of 148 mm. Hence the next step was to create multiple arc treatment tracks simultaneously in the same reactor.

To achieve this aim a design and build process was initiated. The first step was to list the known factors effecting the arc reactor, and then design the reactor to avoid these issues. The issues identified were as follows;

1. Method for initiating the arc
2. Stable anode support
3. Reliable fabric movement rate
4. Eliminate arcs down–line of arc, to avoid smouldering
5. Suppress smouldering in carbon material after the arc via cooling or fuel suppression
6. Develop method to automatically control the arc gap to acceptable accuracy
7. Maintain reactor body at a stable temperature
8. Extract exhaust gases from reactor without causing arc instability

The reactor thus designed consisted of 10 arcs, in groups of two. Each set of two was positioned 75 mm apart across the felt, with five such groups along the felt in the machine direction. These groups were staggered such that there was an arc every 15 mm across the felt. Electrical current was supplied via 10 Enatel rectifiers, sharing a common positive terminal.

3.6.1 Electrical contact

Figure 3.5: Electrical contact, VI arc reactor

3.6.2 Extraction

The initial design for extraction of gas from the arc reactor chamber was via the use of hoods attached to the entrance and exit of the chamber. The rate of extraction was adjustable via the

use of lengths of pipe, the orientation of which either opened or closed holes in the extraction pipes, see figure 3.6.

Figure 3.6: Adjustable rate extraction hood used in VII arc reactor

3.6.3 Vacuum heads

3.6.4 Felt position

The initial design of the entrance and exit feed rollers had a convex profile. This design increased the tension in the middle of the felt. The felt then in theory adjusted its position when moving to equalise the tension across the width, hence aligning its position to the centre of the roller. This system was designed for textiles that exhibit crimp, that is the ability to stretch due to looseness in the weave. A felt does not stretch via this mechanism, but rather stretching is due to fibres straightening or slipping. Hence this solution did not work.

The next trial was with an angled roller. This system was successful, but the position of the rollers required constant adjustment. A automated solution was then acquired see figure 3.7. This solution worked by sensing the edge of the material. The angle of the rollers is then adjusted to keep this edge at the set position. This solution worked.

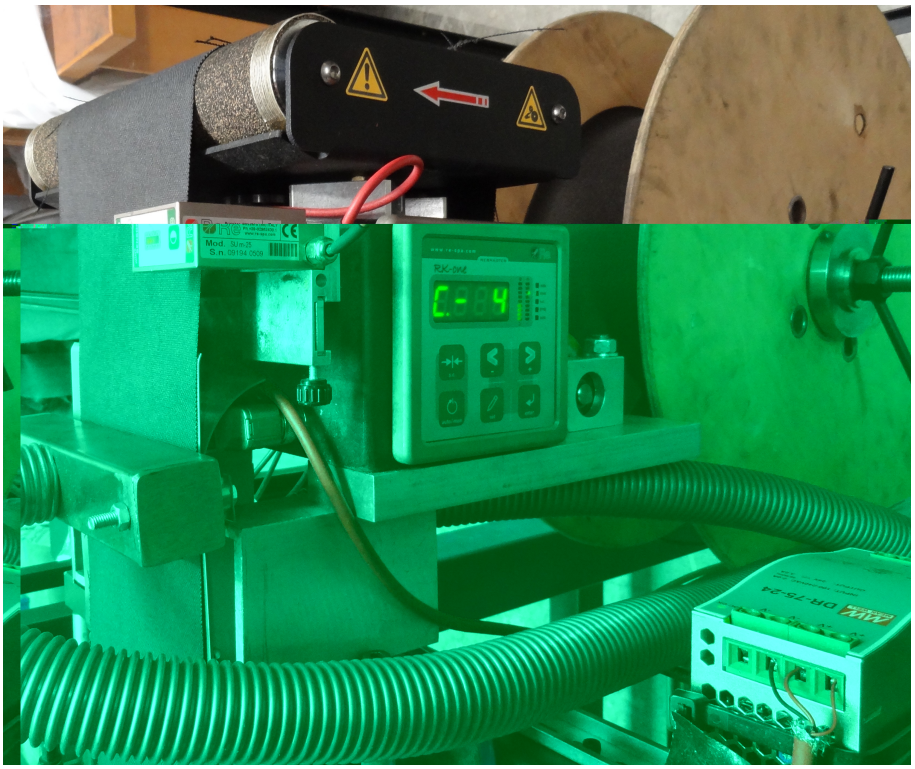

Figure 3.7: Felt position controller

3.6.5 Arc gap

An important factor effecting the treatment of the anode material is the arc gap. Larger gaps produced wider tracks, i.e. 25 mm at 9 mm or greater arc gap compared to 12 mm at 5 mm arc gap. Increasing the arc gap beyond 9 mm does not produce a wider track, but also comes with reduced arc stability. Hence it was important to maintain the arc gap at a minimum of 9 mm, without deviating significantly, defined at 1 mm greater.

Chapter 4

Results

4.1 Felt Parameters

The mean diameter and distribution of the fibres was measured by a diameter analyser (OFDA). This was conducted by the New Zealand Wool Testing Authority Ltd, with the results as follows for the SGL PAN felt used in this work.

mean diameter = 9.1 [μm]
stdev = 2.0 [μm]
cv % = 21.6
number of fibres measured = 12887

4.1.1 Orientation parameter Z

A important modelling parameter was the orientation of the fibres. This parameter Z represents the fraction of fibres orientated normal to the felt surface. It can have values of Z = 0.66 for fibres of random orientation, through to Z = 1 for fibres aligned normal to the felt surface. The influence of this parameter on the model was discussed in section 2.4.1.

The felt used in this work was a needled felt. Hence the orientation was unknown, as carding will have aligned fibres in the lengthwise direction (Gårdmark and Mårtensson, 1966), while needling aligned some of the fibres normal to the surface. To find the correct value for this parameter the maximum temperature on the non–arc side of the felt was found at different value for Z. The correct value was then that at which this temperature was that recorded using the pyrometer.

The model was then used to predict this temperature for SGL felt at 2.7mm thick, and moving at a rate of 5 mm s^{-1}. This value was then recorded and plotted against Z, this plot is given as figure 4.1. The value for Z is then that which gives a maximum temperature on the non–anode side of the felt of 1280 $\pm$ 50 °C. This was found to be a Z value of 0.76.

This value indicates a largely random orientation to the fibres, normal to the felt surface. This was largely expected, if one examines figure 1.9 the fibres appear largely random. That the value was not completely random was due to the effect of needling, which aligned some of the fibres normal to the felt surface (due to the barbs pulling and pushing some fibres in the needled direction).

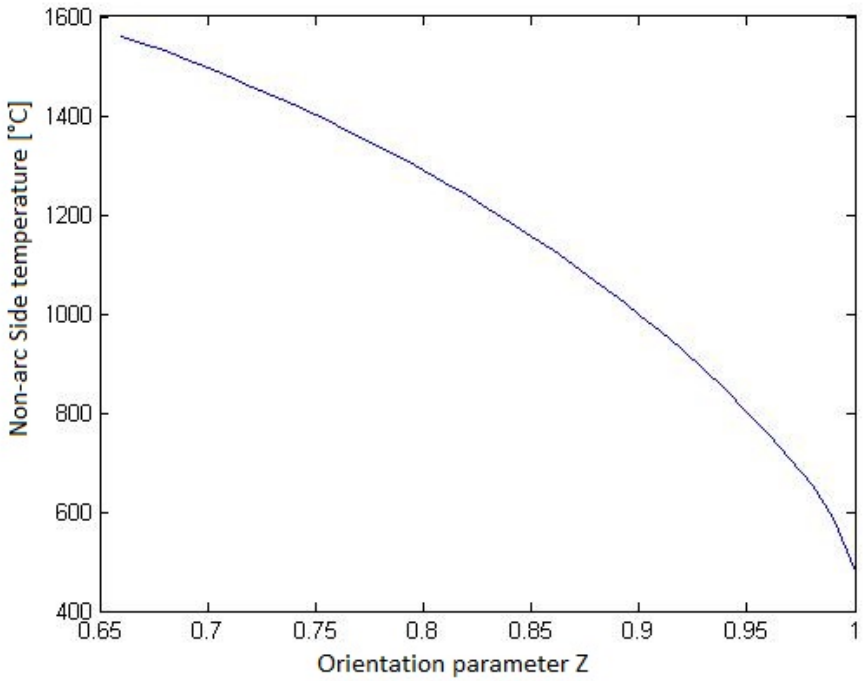

Figure 4.1: Temperature at the cold side of the felt, with varying fibre orientation

4.1.2 Modified Rayleigh number

An important assumption used in the development of the model used in this work was that of negligible natural convection (see section 2.3.2). This assumption was that natural convection can be ignored in the felt if the Rayleigh number is below a value of 13.4. To check this the Rayleigh number was calculated using equation 2.15, as modified for fibre systems by Bhattacharyya. A Fermi estimation was conducted using values from the textbook Leinhard (2012), with linear

extrapolation to the relevant temperatures. This gave a Rayleigh number of Ra=1×10^{-8}, many orders of magnitude below the threshold for natural convection of Ra$\leq$40.

A Fermi estimation is a method by which the order of magnitude of a number can be quickly found. By this method the exact values of a number are not considered important, rather the "size" of a number is considered. For example 7×10^3 will be used as 1×10^4.

The models used in this work were originally developed to investigate heat transfer in glass fibre insulations. As the permeability of the carbon felt is much lower than that of glass fibres, 1.2×10^{-10} m^2 (Luo et al., 2012), compared to $2 - -7 \times 10^{-8}$ m^2 (Wilkes and Graves, 1993), natural convection is greatly reduced. Another factor is the density of air, as the temperature increases this decreases; in equation 2.15 the square of density is used, greatly enhancing this effect. The code for this calculation is given in Appendix .1.5.

4.2 ODE Algorithm

The software used to run the model developed was MATLAB R2011b, a package designed to manipulate matrices. The method used is the method of lines, as described in section 2.2.2.

The method of lines works by replacing the PDEs with algebraic approximations. These can be of three forms, forward, central or backwards, as given by equations 2.2 to 2.4. The only variable left is typically time. The system is then divided up into segments between each boundary; this is then numerically integrated forward in time.

Matlab has two commonly used algorithms for this task (Shampine et al., 2003), ODE 15s, and ODE 45. These algorithms are discussed in further detail in section 2.2.3. Hence a test was necessary to determine which solver would be the optimal for this work.

The test chosen was to compare the time and number of function evaluations of the two algorithms. This involved running the DAEs system at a range of different conditions. The variable chosen was v, the movement rate of the felt through the reactor. This was chosen as it was expected to have the largest effect on the performance of the algorithms involved.

The other variables used for this test are given in table 4.3. While tspan the duration over which the model was run was given as equation 4.1. Where dy the size of a segment along the machine direction of the felt, as used in the method of lines was define as in equation 4.2. This is the distance travelled during tspan.

Felt movement rate [mm s^{-1}]									
0.1		1		5		10		100	
T	n	T	n	T	n	T	n	T	n
5.44	305	3.86	203	2.95	152	2.53	127	1.56	66
2.03	95	1.57	63	1.26	41	1.21	35	1.05	28
2.07	96	1.50	60	1.25	42	1.18	35	1.04	25
2.08	96	1.57	63	1.28	42	1.19	35	0.98	24

Table 4.1: ODE 15s, solution times for model presented

Felt movement rate [mm s^{-1}]									
0.1		1		5		10		100	
T	n	T	n	T	n	T	n	T	n
221.26	45475	21.94	4483	4.28	895	2.28	451	0.39	79
221.23	45589	22.05	4549	4.18	865	2.11	43	0.30	61
219.93	45499	22.17	4579	4.48	925	2.26	469	0.29	61
221.12	45589	22.02	4549	4.39	901	2.12	439	0.30	61

Table 4.2: ODE 45, solution times for model presented

$$\text{Tspan} = \frac{\text{dy}}{\text{v}} \tag{4.1}$$

$$dy = \frac{(\text{dpre} + \text{darc} + \text{dpost})}{{}^{\text{dF}}/_{\text{n R}}} \tag{4.2}$$

The effect of defining the solution time this way was to change the number of times each solver was run. As the rate increased the number of integration steps increased while the time over which each step was integrated reduced. Hence the time over which the solver has to integrate is dependent on the movement rate chosen.

The time taken to find a solution is a combination of both the integration time, and the set–up time. As the integration time decreased the ratio of these two times changed. Hence at higher rates the set–up time became a large portion of the total time, the effect of which was to produce a non–linear plot between integration time and set–up time.

This effect can be seen in figure 4.2, where there is a deviation from linear at the lower end. As the solution time with the use of sparsity has a lower integration computation cost in comparison to set–up cost at lower integration times the set–up cost can be observed.

Over the range of situations trialled ODE 15s is the better algorithm for solving the system of DAEs presented. At a rate of 0.1 mm s^{-1} this difference is of two orders of magnitude, 2.3 s

n = 30	Number of segments
R = 1	Ratio of size of segments through and along section
Tamb = 20	Ambient temperature [°C]
darc = 15	Diameter of arc [mm]
dpre = 10	Model distance before arc [mm]
dpost = 10	Model distance after arc [mm]
dcontact = 2	Width of anode support contact [mm]
dF = 2.7	Felt thickness[mm]
I = 16	Arc current [A]
rho = 3	Felt resistivity [Ω mm]

Table 4.3: Modelling parameters used in ODE comparison tests

compared to 221 s for ODE 45. This difference becomes less as the rate is increased, however at 5 mm s^{-1} (the rate at which the equipment is run) this difference is still three times, 1.25 s compared to 4.40 s for ODE 45. It is worth noting that this time difference is largely mirrored by the number of function calls. These tables indicate that for the system of DAEs used in this study ODE 15s is better than ODE 45.

4.3 Sparsity tests

A sparsity matrix was used to reduce computation time. This took the form of a Jacobian matrix with non–zero elements at the positions at which it was necessary to evaluate the derivative.This is explained further in section 2.2.4 specifically equation 2.8 on page 19. The modelling approach utilises a technique known as method of lines which is explained further in section 2.2.2. The effect of this is that the derivative matrix to be solved grows as the square of the number of segments. To double the accuracy the solver must solve four times the number of equations, with sparsity this greatly reduced the number of equations that must be solved. The sparsity matrix makes the number of equations grow proportionally to the accuracy. As high accuracy is desirable this was greatly beneficial.

It was necessary to compare the effect of sparsity on the different solvers available, in order to fully evaluate which would work best for the model developed. The parameter of importance was the time taken per integration step, as this is the most computative portion of the algorithm. In order to test this effect the model was evaluated over a model time of 3 s, and the time taken to achieve this at a range of different parameters was recorded. The variables used were the same as that used in the tests conducted in section 4.2 with the addition of the variable of whether sparsity was utilised or not.

It was necessary to compare the effect of using sparsity, the results of which can be seen in figures 4.2 and 4.3. tables 4.1 and 4.4. The model was solved via the same ODE solver running in MATLAB for both tests, the difference between the tests was the use of a Jacobian matrix as per equation 2.8. This Jacobian is used to indicate to the solver which values are non–zero, greatly reducing the number of equations that need to be evaluated.

Felt movement rate [mm s^{-1}]									
0.1		1		5		10		100	
T [s]	n	T [s]	n	T [s]	n	T [s]	n	T [s]	n
1366.21	50309	995.64	33539	869.20	25154	743.88	16795	488.75	8400
416.01	8429	320.83	8397	260.25	8375	259.84	8369	280.50	8362
443.07	8430	314.70	8394	261.22	8376	261.48	8369	257.07	8359
442.68	8430	336.71	8397	256.78	8376	266.87	8369	255.19	8358

Table 4.4: Solution time taken for ODE 15s, without sparsity

A direct comparison of tables 4.1 and 4.4 gives an indication of the improvement due to the sparsity matrix. Where T was the time taken per integration step, for the n number of Jacobian evaluations. The effect of which was an improvement of over two orders of magnitude, when comparing the integration time at any rate and step. This improvement was mirrored in the number of function calls, which indicated that the improvement was not solely due to reduced number of equation evaluations. If that had been the case the number of function calls would have been similar between the two tests, with the increase in time taken being due to the number of evaluations required. However it can be seen that the Jacobian matrix evaluations have also increased by a similar ratio.

ODE Solver	Sparse?	Median	95% C.I.	95% C.I.
15s	No	0.032	0.004	11%
15s	Yes	0.025	0.003	13%
45	Yes	0.005	0.004	90%

Table 4.5: Jacobian evaluation rate for different ODE solvers in MATLAB

Sparsity significantly reduced the time taken per Jacobian evaluation for ODE 15s. Table 4.5 shows the time taken per Jacobian evaluation for the three situations trialled. It is apparent that ODE 45 is much faster, 0.005 s per evaluation compared to 0.025 s for ODE 15s. This is as expected as ODE 15s has been designed for stiff systems and is hence computationally more expensive per evaluation. The first two rows of table 4.5 compared ODE 15s with and without the passing into the solver of a sparsity matrix. The results of adding sparsity was an increase of about 30 % in computation time, much less than expected. The main benefit of sparsity was hence the ability of the solver to take larger steps towards the solution.

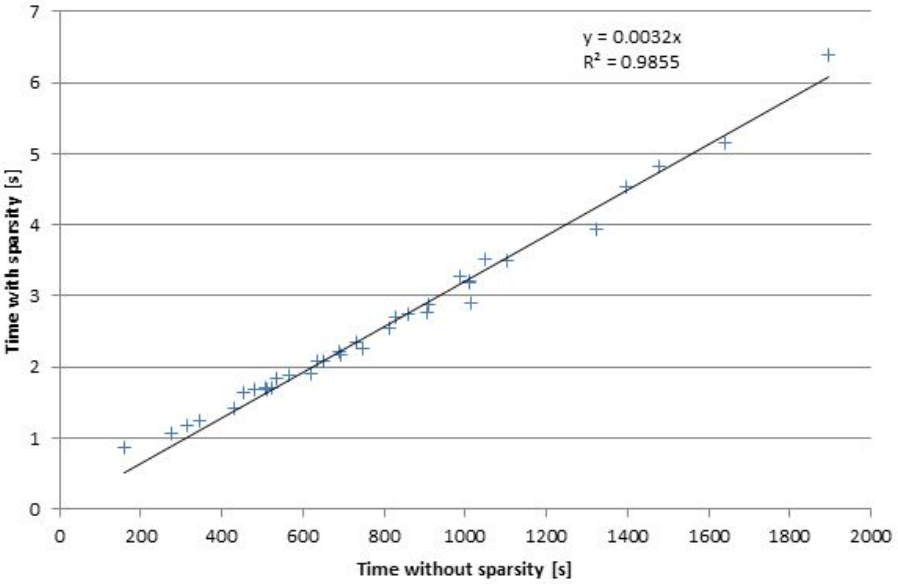

Figure 4.2: Solve time using ODE 15s with and without sparsity

Sparsity had no effect on computation time for ODE 45. Figure 4.3 shows the effect of sparsity on the solution time for ODE 45, with a linear fit indicating a relationship of 1:1. This indicates that ODE 45 did not see an improvement due to sparsity. This was as expected as the algorithm was designed to work best with non–stiff systems, the addition of sparsity can not change the stiffness of the system.

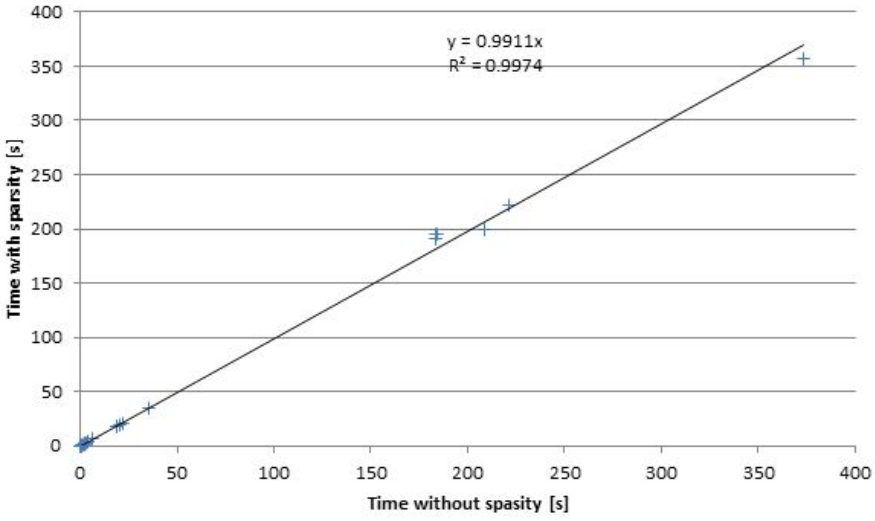

Figure 4.3: Solve time using ODE 45 with and without sparsity

4.4 Felt thermal profiles

The model tracks elements in the felt as they pass through the arc, starting 10 mm before the arc, to 150 mm after then arc. This profile is symmetrical about the centreline of the arc in the machine direction consisting of two physical dimensions, temperature, graphitisation degree, and vaporisation rate recorded against time. This model was used at multiple movement rates. A felt movement rate of 3 mm s^{-1} was used as that is the rate that was historically used in the arc reactor, described in section 3.1.2. The standard rate as of November 30, 2014was 5 mm s^{-1}, this was also modelled. The movement rates of 10 mm s^{-1} and 15 mm s^{-1} were also modelled, as these have been used in testing.

Figures 4.4 to 4.12 are given in the following pages. They show the thermal history of the felt, at the arc side, at the middle, and at the cold non–arc side. Temperatures are displayed on the y–axis, while the x–axis displays the time scale. In the first set 30 s being displayed. This tracks the temperature of a finite element as it passes through the arc; starting 10 mm before the arc. Therefore the stationary arc is encountered by the element at different times at the four rates modelled, this time is given below.

movement rate		arc time
3 mm s^{-1}	=	$3\frac{1}{3}$ s
5 mm s^{-1}	=	2 s
10 mm s^{-1}	=	1 s
15 mm s^{-1}	=	$\frac{2}{3}$ s

Figures 4.7 to 4.9 show the same data over 10 s. This allows closer examination of transient behaviour, with heating rates observable. Figures 4.10 to 4.12 display the thermal data of a finite element over 150 mm. This allows direct observation of the thermal response at three different positions within the felt. The distance of 150 mm was used as this correlated to the spacing of the arcs in the machine direction of the felt as described in section 3.6.

Figure 4.4 illustrates the time history over 30 s of the carbon felt at different movement rates, at the arced face. It can be seen that the influence of increasing speed is to change the duration of the time at high temperatures.

Figure 4.5 illustrates the equivalent time history of the carbon felt at different movement rates, halfway through. It can be seen that the role of increasing movement speed is also to reduce the peak temperature. This effect is due to the decreased time at which the arc side was exposed to the high temperature of the arc. As the heating rate was similar (gradient of each line), this peak therefore took longer to achieve at lower rates. The result of which was the fabric maintaining

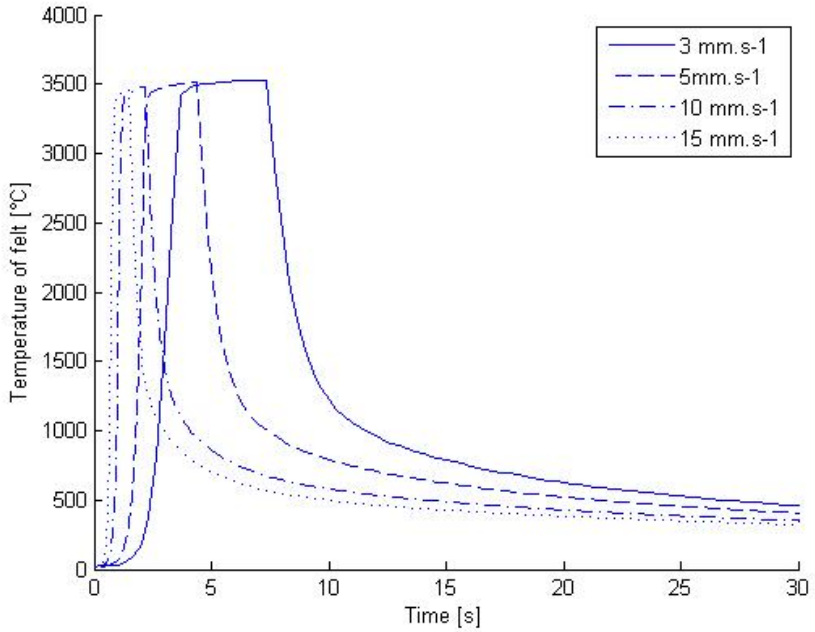

Figure 4.4: Thermal profile of arc side of felt over 30 s, at multiple movement rates

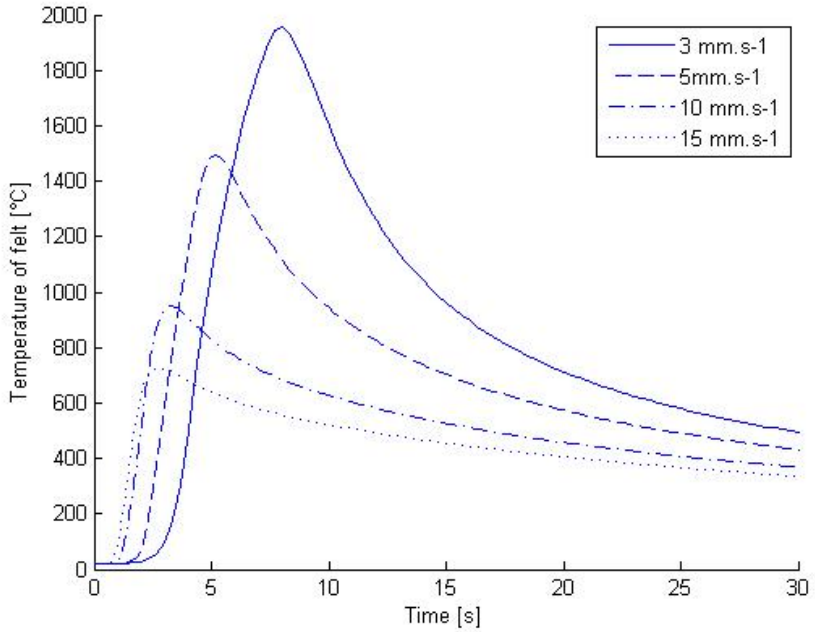

Figure 4.5: Thermal profile of middle of felt over 30 s, at multiple movement rates

an elevated temperature for longer.

Figure 4.6 illustrates the equivalent time history of the carbon felt at different movement rates,

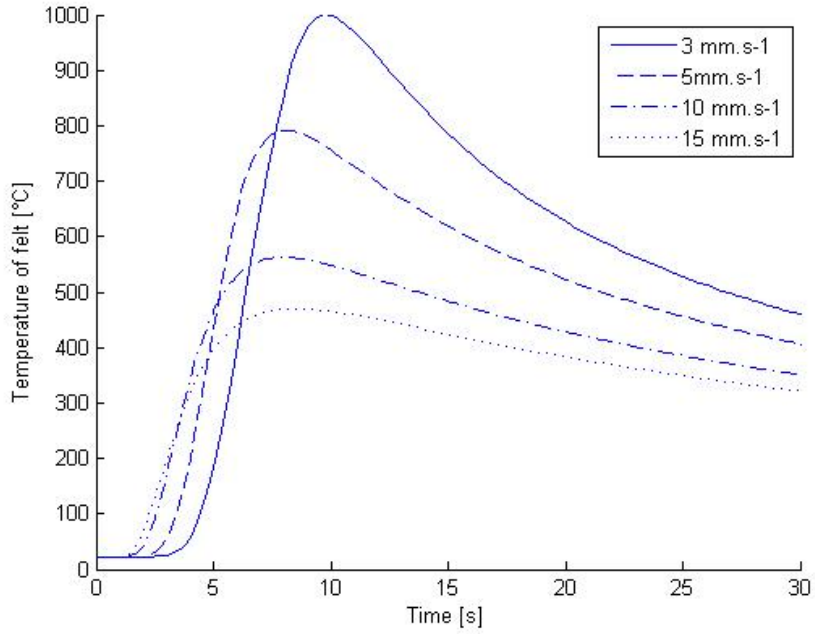

Figure 4.6: Thermal history of cold side of felt over 30 s, at multiple movement rates

at the face on the opposite side from the arc. It can be seen that the role of increasing movement speed is similar to what occurred in the middle of the felt. However it is evident that the heating rate is lower. While temperature gradients up to 300 °Care similar, this rate decreases at higher temperatures, due to radiative heat loss. The cold side the surroundings are at a constant lower temperature (see section 3.6, where the reactor body is maintained at a constant temperature). The time of this peak is delayed from that at the centre, due to movement of the felt. It can be seen from figure 4.6 that at higher movement rates this peak is very flat.

Figure 4.7 illustrates the time history of the carbon felt at different movement rates, at the arc side over 10 s. In this figure the heating time at each rate can be observed, with the felt heating over about 1 s at a rate of 3 mm s^{-1}, compared to about 0.25 s at 15 mm s^{-1}.

Figure 4.8 illustrates the time history of the carbon felt at different movement rates, at middle of the felt over 10 s. In this figure the heating time at each rate can be observed, this rate if similar above 200 °C. This effect is due to decreased heating rate at the cold side countering the increased rate at the hot arc side.

Figure 4.9 illustrates the temperature history of the carbon felt at different movement rates, at the cold non–arc over 10 s. In this figure the heating time at each rate can be observed, with increased movement rate resulting in reduced heating rate.

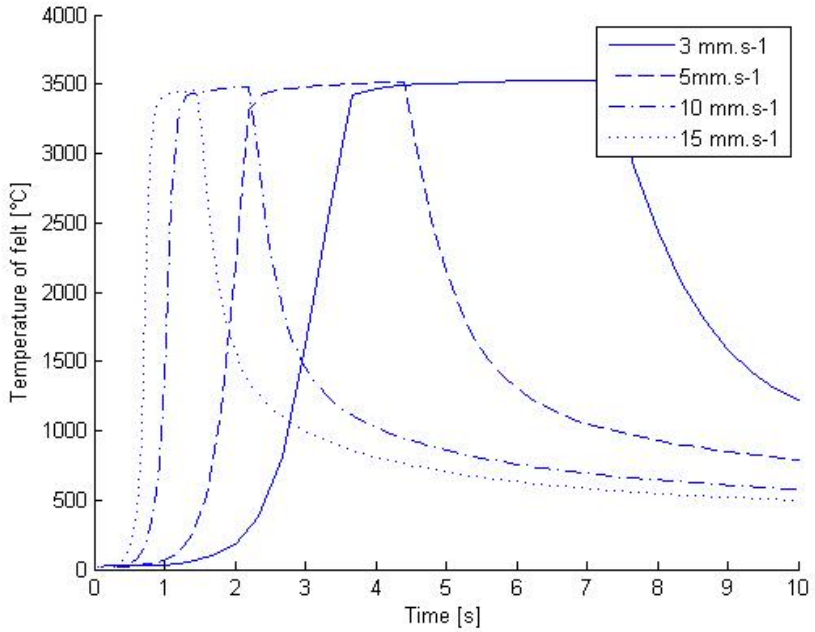

Figure 4.7: Thermal history of arc side of felt over 10 s, at multiple movement rates

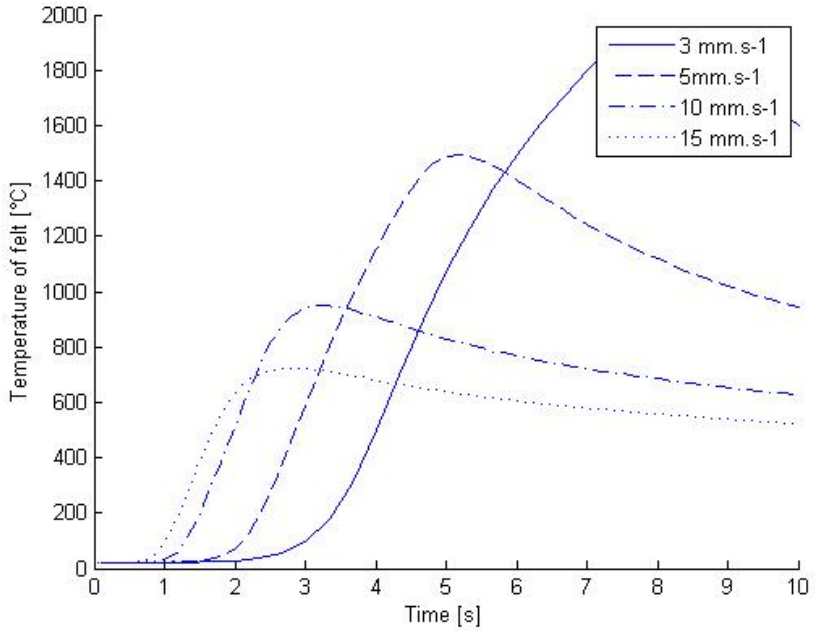

Figure 4.8: Thermal history of middle of felt over 10 s, at multiple movement rates

Figure 4.10 illustrates the temperature history of the carbon felt at different movement rates, at the arc over 150 mm. It can be seen that effect of movement rate is not as strongly influential as when displayed over time. The thermal profile through the arc is similar at all rates, with the

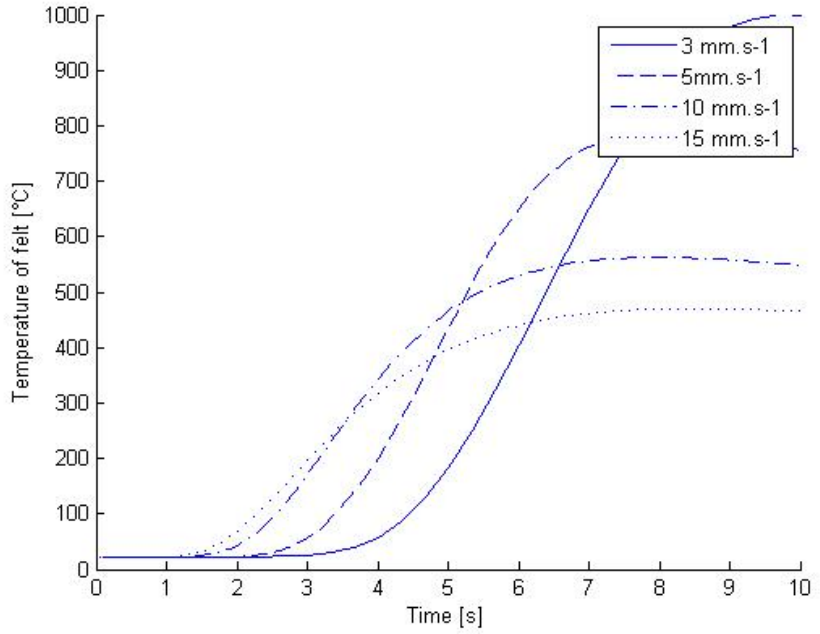

Figure 4.9: Thermal history of cold side of felt over 10 s, at multiple movement rates

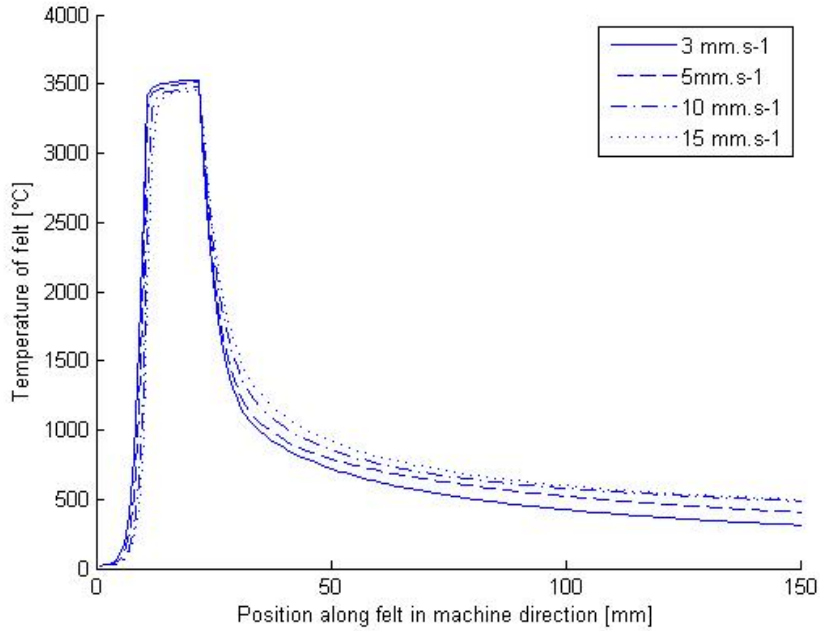

Figure 4.10: Thermal history of arc side of felt over 150 mm, at multiple movement rates

higher rates reaching slightly reduced peak temperature. The felt is also at an elevated (compared to ambient) temperature for a long distance. In figure 4.4 the felt cools faster at higher rates it can be seen in figure 4.10 that a higher temperature is maintained up to the next arc station.

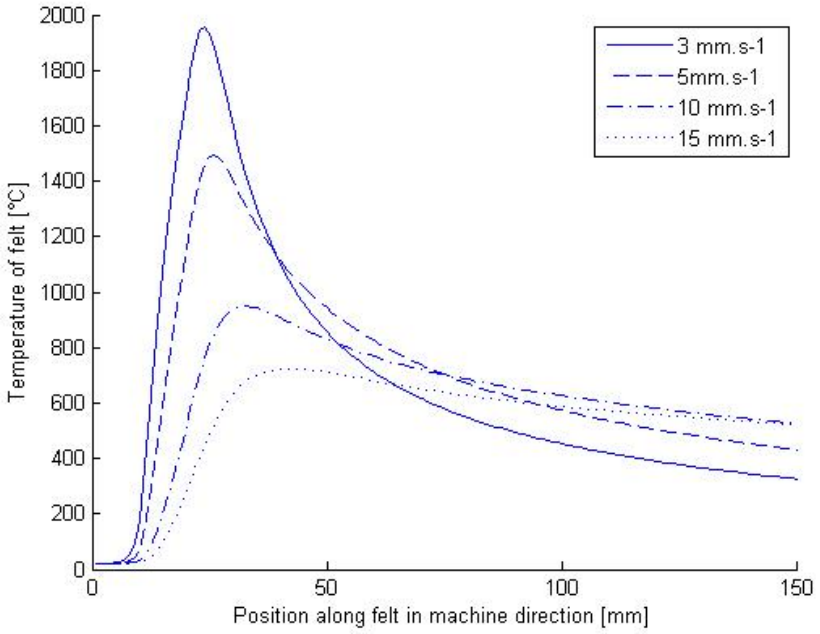

Figure 4.11: Thermal history of middle of felt over 150 mm, at multiple movement rates

Figure 4.11 illustrates the temperature history of the carbon felt at different movement rates, at the middle over 150 mm. It can be seen that at higher movement rates the thermal peak is off–set further in the machine direction, while this peak occurs in a shorter time the increased rate counters this effect. Figure 4.12 illustrates the time history of the carbon felt at different movement rates, at the cold non–arc over 150 mm. It can be seen that the location of the thermal peak is strongly dependant on the movement rate. This is what has been observed in practice.

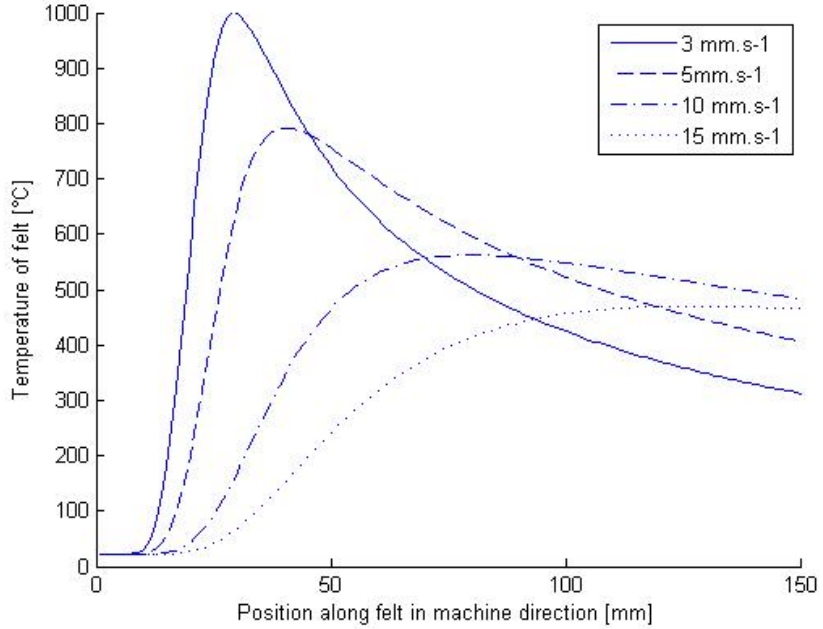

Figure 4.12: Thermal history of cold side of felt over 150 mm, at multiple movement rates

Chapter 5

Conclusions and Future Directions

In this study a model of the heat transfer into a carbon felt anode was created. This was then used to create a thermal history of the felt. Using this history the graphitisation and vaporisation kinetics where used to predict changes due too these mechanisms.

From the predicted thermal profile the change in degree of graphitisation was found to be minimal beyond about 0.3 mm into the felt from the arc side. While the vaporised carbon was predicted to be enough to cover all the felt fibres with many graphene layers. This modified surface chemistry was expected to explain the performance observed.

In conclusion it was found that the mechanism explaining the performance of an Arcactive battery was likely to be vaporisation and deposition of carbon.

Future work may involve the investigation of the carbon surface after arc treatment. To investigate for changes from PAN structure to that of graphene or other carbon forms, such as esters.

Bibliography

J. Abrahamson, C. Davies, J. Stott, R. Ward, and P. Wiles. Erosion rates of graphite anodes in high current arcs. *Ind. Eng. Chem. Fundam*, 19:223–243, 1980.

M. T. Azarova and M. E. Kazakov. World production and consumption of carbon fibres. *Fibre Chemistry*, 42:271–277, 2011.

Z. Bashir. A critical review of the stabilisation of polyacrylonitrile. *Carbon*, 29(8):1081–1090, 1991.

R. K. Bhattacharyya. Heat-transfer model for fibrous insulations. *Thermal Insulation Performance, ASTM STP*, 718:272–286, 1980.

Hamdan bin Mohamed Yusoff. *Continuous Production of Carbon Nanotubes using Carbon Arc Reactor: Anode Surface Temperature Study and CFD Modelling*. PhD thesis, University of Canterbury, 2008.

H. S. Carslaw and J. C. Jaeger. *Conduction of heat in solids*. Clarendon Press, Oxford, 4 edition, 1976.

N. K. Chaney, V. C. Hamister, and S. W. Glass. The properties of carbon at the arc temperature. *Transactions of the Electrochemical Society*, 67:107–151, 1935.

C. Davies and J. Abrahamson. Limit to erosion rate in a high-current carbon arc. *Ind. Eng. Chem. Process Des. Dev.*, 22:226–230, 1983.

C. J. Erickson. *Handbook of Electrical Heating for Industry*. IEEE Press, New York, U.S.A, 1 edition, 1995.

E. Fitzer and S. Weisenburger. Kinetics of graphitization within the first minute of heat treament. *Carbon*, 14:323–321, 1976.

H. Fricke. A mathematical treatment of the electric conductivity and capacity of disperse sys-

tems i. the electric conductivity of a suspension of homogeneous spheroids. *Phys. Rev.*, 24: 575–587, Nov 1924.

L. Gårdmark and L. Mårtensson. An experimental investigation of fiber orientation and some properties of needled felts. *Textile Research Journal*, pages 1037–1042, 1966.

M. L. Greene, R. W. Schwatrz, and J. W. Treleaven. Short residence time graphitization of mesophase pitch-based carbon fibres. *Carbon*, 40:1217–1226, 2002.

R Hemmi, Y Yokomizu, and T Matsumura. Anode–fall and cathode–fall voltages of air arc in athmosphere between silver electrodes. *Journal of Physics D: Applied Physics*, 36:1097–1106, 2002.

H. Hertz. Über die berührung fester elasticher körper. *J. Reine Angew. Math*, 29:156–171, 1882.

N. Hollen and J. Saddler. *Textiles*. 4. The MacMillan Company, New York, 2 edition, 1965.

D. K. Joshi and S. P. Sukhatme. Convective heat transfer within fibrous insulation slabs. *Wårme– und Stoffübertragung*, 3:183–190, 1973.

M. G. Kaganer. Thermal insulation in cryogenic engineering. *Israel Program for Scientific Translations*, 1969.

Y. Kirizbaeva, B. E. Geller, and K. Volkna. a. *Fibre Chemistry*, 5:39–40, 1981.

J. H. Leinhard. *A Heat Transfer Textbook*. Philogston Press, Massachusetts, U.S.A, 4 edition, 2012.

F. Llewellyn-Jones. *Ionization and Breakdown in Gases*. Fletcher and Son LTD, Norwich, England, 2 edition, 1966.

C. J. Luo, S. D. Stoyanov, E. Stride, E. Pelan, and M. Edirisinghe. Electrospinning versus fibre production methods: from specifics to technological convergence. *Chem. Soc. Rev.*, 41: 4708–4735, 2012.

J. Mittal, O. P. Bahl, and R. B. Mathur. Single step carbonization and graphitization of highly stabilized pan fibers. *Carbon*, 35:1196–1197, 1997.

E. Nasser. *Fundamentals of Gaseous Ionization and Plasma Electronics*. John Wiley & Sons INC, New York, U.S.A, 1 edition, 1971.

G. H. Oelsner. *A Handbook of Weaves*. Dover Publications, Inc, 1953.

K. E. Perepelkin. Carbon fibres with specific physical and physicochemical properties based on

hydrated cellulose and polyacrylonitrile precursors. a review. *Fibre Chemistry*, 34(4):271–280, 2002.

M. S. A. Rahaman, A. F. Ismail, and A. Mustafa. A review of heat treament on polyacrylonitrile fiber. *Polymer Degradation and Stability*, 92:1421–1432, 2007.

N. A. Sanders and E. Pfender. Measurement of anode falls and anode heat transfer in atmospheric pressure high intensity arcs. *Journal of Applied Physics*, 55(3):714–722, 1984.

C. Sauder, J. Lamon, and R.Pailler. Thermomechanical properties of carbon fibres at high temperatures up to 2000c. *Composites Science and Technology*, 62:499–504, 2001.

W. E. Schiesser and G. W. Griffiths. *A Compendium of Partial Differential Equation Models Method of Lines Analysis with Matlab*. Cambridge University Press, New York, U.S.A, 1 edition, 2009.

L. F. Shampine, I. Gladwell, and S. Thompson. *Solving ODEs with MATLAB*. Cambridge Universtiy Press, New York, U.S.A, 1 edition, 2003.

Z. Shuyan, Z. Boming, and D. Shanyi. Effects of contact resistance on heat transfer behaviors of fibrous insulations. *Chinese Journal of Aeornautics*, 22, 2009.

J. M. Somerville. *The Electric Arc*. John Wiley & Sons INC, New York, U.S.A, 1 edition, 1959.

N. Sonobe, T. Kyotani, and A. Tomita. Carbonization of polyacrylonitrile in a two–dimensional space between montmorillonite lamellae. *Carbon*, 26:573–578, 1988.

C. Stark and J. Fricke. Improved heat-transfer models for fibrous insulations. *Int. J. Heat Mass Transfer*, 36(3):617–625, 1993.

J. S. Townsend. *The Theory of Ionization of Gases by Collision*. Constable & Company LTD, London, England, 1 edition, 1910.

P. G. Wiles and J. Abrahamson. Carbon fibre layers on arc electrodes - their properties and cool-down behaviour. *Carbon*, 16:341–349, 1978.

K.E Wilkes and R. S. Graves. Air–flow permeability of attic insulation materials. 1993.

A. V. Wouwer, P Saucez, and W. E. Schiesser. *Adaptive method of lines*. CRC Press LLC, Florida, U.S.A, 1 edition, 2001.

K. Yamazaki, E. Yamamoto, K. Suzuki, F. Koshiishi, K. Waki, S. Tashiro, M. Tanaka, and K. Nakata. The measurement of metal droplet temperature in gma welding by infrared two-colour pyrometry. *Journal of Applied Polymer Science*, 26(3):81–87, 2009.

D. Zheng, G. Baciu, and J. Hu. Accurate indexing and classification for fabric weave patterns using entropy-based approach. *Proc. 8th IEEE Int. Conf. on Cognitive Informatics*, 2009.

Appendices

.1 Matlab Code

.1.1 Matlab Graphitization

```
function Graphfit
%Program fit kinetics for graphitization
%Created by Hannu Out 17-02-14
for i=1:4
    delete(gcf)
end
global c_20 tspan
Temp=[1860, 2090, 2250, 2500]; %Temperature to fit at °C
Arr=[1.2e20]; %Pre exponential factor to fit
for i=1:length(Temp)
    C(i,1,:)=graphitizationdegree(Temp(i),Arr(1));
end
[x ~ z]=size(C);
time=tspan/60;
for i=1:x
    p(i,:)=C(i,1,:); %Spacing
    contrac(i,:)=c_20-p(i,:);    %Contraction
end
hold on
for k = 1:x
    plot(time,contrac(k,:));
end
%Data from Fitzer 76
%1860, 2090, 2250, 2500
%0.007, 0.018, 0.036, 0.069 -contraction from zero?
plot(10,0.007,'o',10,0.018,'+',10,0.036,'x',10,0.069,'x')
set(gca,'xscale','log','YDir','reverse')
axis tight
xlabel('log(time) mins')
ylabel('contraction')
hold off
```

```
function C=graphitizationdegree(Temp,Arr)
%Program to calculate degree of graphtization of time at a
%set temperature
%Created by Hannu Out 14-02-14
global deltaE A R c_20 c_2inf T tspan c_2
A=Arr;
T=Temp;
deltaE=268; %Activation energy [kcal/mol]
deltaE=deltaE*4184; %Convert to J/mol
R=8.314;    %Gas constant
%Graphitization
c_20=3.44;  %Spacing carbon
c_2inf=3.354;   %Spacing graphite
c_2=3.432; %Initial spacing
T=T+273; %Convert to Kelvin
tspan=[0:.1:20*60];
options=odeset('abstol',1e-6,'reltol',1e-6);
[t,C]=ode15s(@dcdt,tspan,c_2,options);
end
function dcdt=dcdt(t,C)
global deltaE A R c_2inf T c_20
k=A*exp(-deltaE/(R*T)); %Reaction rate
Deg=(1-(C-c_2inf)/(c_20-c_2inf));
Rem=1-Deg; %Fraction to be graphitized
dcdt=-Rem*k;     %Change in spacing
end
```

.1.2 Matlab Variable Z

.1.3 Matlab Derivative function

```
function dEdt=dTdtdcdt(t,T)
%Function to calculate the algebraic approximation to the derivative
%Created by Hannu Out
global lambdasga lambdasgb sigma e dx  n m Tsidea Tsideb Tsidec dy ep mem
E=4*10e4;  %Carbon Black, Rosseland mean extinction coefficient
ni=2;        %Average index of refraction
Temp=reshape(T(1:m*n),m,n);
%Average temperature of radiation
%First
Tra(:,1)=((Tsidea+Temp(:,1)).*(Tsidea.^2+Temp(:,1).^2)/4).^(1/3);
%Bulk
Tra(:,2:n)=((Temp(:,1:n-1)+Temp(:,2:n)).*(Temp(:,1:n-1).^2+Temp(:,2:n)...
    .^2)/4).^(1/3);

%First
Trb(1,:)=((Temp(1,:)+Tsidec).*(Temp(1,:).^2+Tsidec.^2)/4).^(1/3);
%Bulk
Trb(2:m,:)=((Temp(1:m-1,:)+Temp(2:m,:)).*(Temp(1:m-1,:).^2+Temp(2:m,:)...
    .^2)/4).^(1/3);

lambdarada=16*ni^2*sigma*Tra.^3/(3*E);
lambdaradb=16*ni^2*sigma*Trb.^3/(3*E);

%Through
%Cold
dEdta(:,n)=(lambdasga+lambdarada(:,n)).*(Temp(:,n-1)-Temp(:,n))/dx...
    -1*sigma*e*Temp(:,n).^4+sigma*e*Tsideb.^4;
%Hot
dEdta(:,1)=-(lambdasga+lambdarada(:,1)).*(Temp(:,1)-Temp(:,2))/dx...
    -1*sigma*e*Temp(:,1).^4+sigma*e*Tsidea.^4;
%Middle
dEdta(:,2:n-1)=(lambdasga+lambdarada(:,2:n-1)).*(Temp(:,1:n-2)-Temp(:,...
    2:n-1))/dx...
    -(lambdasga+lambdarada(:,3:n)).*(Temp(:,2:n-1)-Temp(:,3:n))/dx;


%Lenghtwise
dEdtb(2:m-1,:)=(lambdasgb+lambdaradb(2:m-1,:)).*(Temp(1:m-2,:)-Temp(2:...
    m-1,:))/dy...
    -(lambdasgb+lambdaradb(3:m,:)).*(Temp(2:m-1,:)-Temp(3:m,:))/dy;
dEdtb(1,:)=...
    -(lambdasgb+lambdaradb(1,:)).*(Temp(1,:)-Temp(2,:))/dy; %Symmetric
%     (lambdasgb+lambdaradb(1,:)).*(Tsidec-Temp(1,:))/dy...
dEdtb(m,:)=...
    -(lambdasgb+lambdaradb(1,:)).*(Temp(m,:)-Temp(m-1,:))/dy; %Symmetric
% (lambdasgb+lambdaradb(m,:)).*(Tsidec-Temp(m,:))/dy...
dEdtc=dEdta+dEdtb+ep;
dEdt=reshape(dEdtc,m*n,1);
```

```
49 -    mem=mem+1;
50
51 -    global deltaE k0 R c_2inf graph c_20
52 -    if graph==1
53      %rate of change of concentration
54 -    k(1:m*n)=k0.*exp(-deltaE./(R.*T(1:n*m))); %Reaction rate
55 -    C(1,:)=T(n*m+1:2*n*m); %D002 Spacing
56 -    Deg=(1-(C-c_2inf)/(c_20-c_2inf)); %Degree of Graphitsation
57 -    Rem=1-Deg;  %Degree remaining
58 -    dcdt=-Rem.*k;   %Rate of reaction
59 -    dcdt=reshape(dcdt,m*n,1);
60 -    dEdt=[dEdt ; dcdt];
61 -    end
62 -    end
```

.1.4 Matlab Problem set–up

```
function [T,Cin,dt]=starkmodelBMradzoneZdt(counter,v,Tin,Cin)
% Function to predict the thermal profile, and graphitization degree
% Based on Stark & Fricke Model(based on Battacharyya's model) as described
% in Improved heat-transfer models for fibrous insulations Int. J. Heat
% Mass Transfer Vol.36 No. 3. pp. 617-625, 1993
% Created by Hannu Out
format long
for j=1:4
    delete(gcf)
end

global Z lambdasga lambdasgb Th sigma e Ta dx i rhoc n m Tsidea Tsideb
global dy Tsidec ep mem graph
% Hannu Out
% 08-07-13
global deltaE k0 R c_20 c_2inf
deltaE=268*4184; %Activation energy [kcal/mol]
k0=1.1e20;   %Reaction rate-fitted 18-02-14
R=8.314;    %Gas constant
c_2inf=3.354;   %Spacing graphite
c_20=3.44;  %Spacing of carbon
c_2=3.432; %Spacing at start
lambda0=30; %Thermal conductivity of solid
lambdag=.024;   %Thermal conductivity of gas
Cr=lambdag/lambda0; %Ratio of gas to solid
E=.045;                 %Voidage
rhog=.012;              %Density of gas
rho0=1.6;             %Density of fibre material
rho=E*rho0+(1-E)*rhog;            %Density of specimen

Vr=rho/(rho0-rho);  %Ratio of fibre and gas
Za=.89; %orientation parameter fitted 19-02-14
for i=1:length(Za)
    lambdasg(i)=lambda0*(1+(Cr-1)/(1+Vr*(1+Za(i)*(Cr-1)/(Cr+1))));
end

Zb=.98;
lambdasgb=lambda0*(1+(Cr-1)/(1+Vr*(1+Zb*(Cr-1)/(Cr+1))));
% ---------------------------------------------------------
sigma=5.67e-8;%Stefan-Boltzmann
e=1;        %Emissivity
Th=3850;    %Arc temp
Ta=295;     %Ambient Temp
% Th=Ta;
dF=2.7e-3;  %Felt thickness
rhoc=1600;  %Density of carbon
I=14;       %Arc current [A]
rho=3;      %Resistivity [ohm.mm]
```

```
das=15;     %Distance from arc axis to anode support contact [mm]
dcontact=2; %Contact to anode support
n=5;          %Number of zones
dx=dF/n;        %Thickness of zone
Tmax=100;    %Model time [s]

dpre=500-12-5; %Distance pre arc [mm]
darc=12;        %Diameter of arc [mm]
dpost=5;        %Distance after arc [mm]
d1=0;
d2=dpre*1e-3;
d3=(dpre+darc)*1e-3;
d4=(dpre+darc+dpost)*1e-3;

dy=1e-3;  %Distance incriment, set to same as through felt [m]
m=round(d4/dy); %0-10=pre arc, 10-30=arc, 30-60=post arc

dt=(round(dy/v*10000000)/10000000); %Time step
y0=ones(m,n)*Ta;
C0=ones(m,n)*c_2;
%Electrical Pathway
[ep]=electricalpathwayshape(m,n,darc,dpre,das,dcontact,dy,rho,dF,I);
Tsidea=arctemp(m,dy,d1,d2,d3,d4,Th,Ta)';
Tsideb=y0(:,n);
Tsidec=y0(m,:);
Tsided=y0(1,:);
Cside=C0(m,:);
y0=reshape(y0,m*n,1);   %Set to column vector
C0=reshape(C0,m*n,1);
tol=1e-9;
if graph==1
    Y0=[Tin,Cin];
    options=odeset('RelTol',tol,'JPattern',Jpatterndc(m,n));
else
    Y0=[Tin];
    options=odeset('RelTol',tol,'JPattern',Jpattern(m,n));
end
tspan=(0:dt:dt);
C=C0;
mem=0;
lambdasga=lambdasg(1);
if counter==1
for i=1:length(tspan)
        [o p]=size(Tsurf);
    if i==2 %Movement of matrix
        y0=Tsurf(:,p);
        y0=reshape(y0,m,n);
        y0=[Tsidec;y0(1:m-1,:)];
```

```
97 -            y0=reshape(y0,m*n,1);
98 -            if graph==1
99 -            Cnew1=C(:,p);
100 -           Cnew2=reshape(Cnew1,m,n);
101 -           Cnew3=[Cside;Cnew2(1:m-1,:)];
102 -           Cnew4=reshape(Cnew3,m*n,1);
103 -           y0=reshape(y0,m*n,1);
104 -           Y0=[y0;Cnew4];
105 -           else
106 -               Y0=y0;
107 -           end
108 -       end
109         %Integration step
110 -       [T,Y]=ode15s(@dTdtdcdt,tspan,Y0,options);
111 -       Tsurf=[Tsurf Y(:,1:m*n)'];
112 -       if graph==1
113 -           C=[C Y(:,m*n+1:m*n*2)'];
114 -       end
115 -   end
116 -   [g,w]=size(Tsurf);
117 -   T=Tsurf(:,w);
118 -   if graph==1
119 -       Cin=C(:,w);
120 -   end
121 -   else
122 -       T=y0;
123 -       Cin=C0;
124 -   end
```

.1.5 Matlab Rayleigh number

```
function Rayleigh
% Function to calculate modified Rayleigh Number for SGL felt during arc
% Created by Hannu Out
clc
clear
for i=1:4
    delete(gcf)
end
% g m/s2    gravity
% beta  K-1 coefficient of volume expansion of air
% rho   kg/m3   mass density of air
% Cp    J/kg K  specific heat of air and constant pressure
% K m2  permeability of the solid skeleton
% T K   temperature differenc3e between hot and cold surface
% D m   distance between hot and cold
% mu    Pa.s    dynamic viscosity of air
% k W/m.K   apparent thermal coinductivity of porous medium
g=9.81;
rho1400=.2520;
rho1500=.2352;
beta623=1.61e-3;
beta673=1.49e-3;
Cp1400=1201;
Cp1500=1211;
K=50e-9;
K=1200e-13;
Thot=3850;
Tcold=1200;
dT=Thot-Tcold;
D=3.0e-3;
mu1400=5.403e-5;
mu1500=5.648e-5;
k=70;
% ----------------------------------
T=(Thot+Tcold)/2;
rho=rho1400+(T-1400)*(rho1500-rho1400)/(1500-1400)
beta=beta623+(T-623)*(beta673-beta623)/(673-623);
beta=1e-3
Cp=Cp1400+(T-1400)*(Cp1500-Cp1400)/(1500-1400)
mu=mu1400+(T-1400)*(mu1500-mu1400)/(1500-1400)
Ra=g*(beta*rho^2*Cp)/mu*K/k*dT*D
end
```

.1.6 Matlab Vaporisation

```
53 -    A=29.39255709;
54 -    B=-107825.133;
55 -    rate=exp(A+B./T(1:m*n)); % errosion rate kg.m-2.s-1
56 -    Diameter=T(n*m+1:2*n*m);    %Diameter, tracked variarble
57 -    Area=pi/4*Diameter.^2; %Area m2
58 -    errosion=rate.*Area/1600; %rate in m-3.s-1
59 -    errosion=real(sqrt(errosion*4/pi)); %Unit length, convert to m-1.s-1
60 -    dcdt=reshape(-errosion,m*n,1);
61 -    dEdt=[dEdt ; dcdt];
62 -    end
63 -    end
```

.2 Resistivity

The electrical resistivity of the felt was found by measuring the electrical resistance. The electrical resistance was recorded by a resistance meter(TTi model BS407). This worked by providing a current with one set of connections, and the voltage across another set is then recorded. If these two set of clamps are connected at the same position this is then the resistance. The first set of clamps is called the “force”, while the other are the “sense”.

To find the resistivity the resistance at multiple distances was recorded. By plotting this resistance against the distance the resistivity of the sample could be found, via equation 2.18. In order to record the resistivity reliably a jig was constructed, by which square bars of Aluminium where held parallel to each–other with a standard tension. The spacing of the bars was set via the jig, this resulted in reliable value recorded. This jig is shown in figure 1.

The resistivity of the carbon rods was measured by a similar method. The length of carbon rod supplied by manufacturers (generally 300 mm of either 3 or 6 mm diameter) was clamped at each end by a double contact of a resistance meter and the resistance noted (50 μA current used). Resistance R and length l was used for calculating the resistivity = (R / l).(Cross-sectional area) .

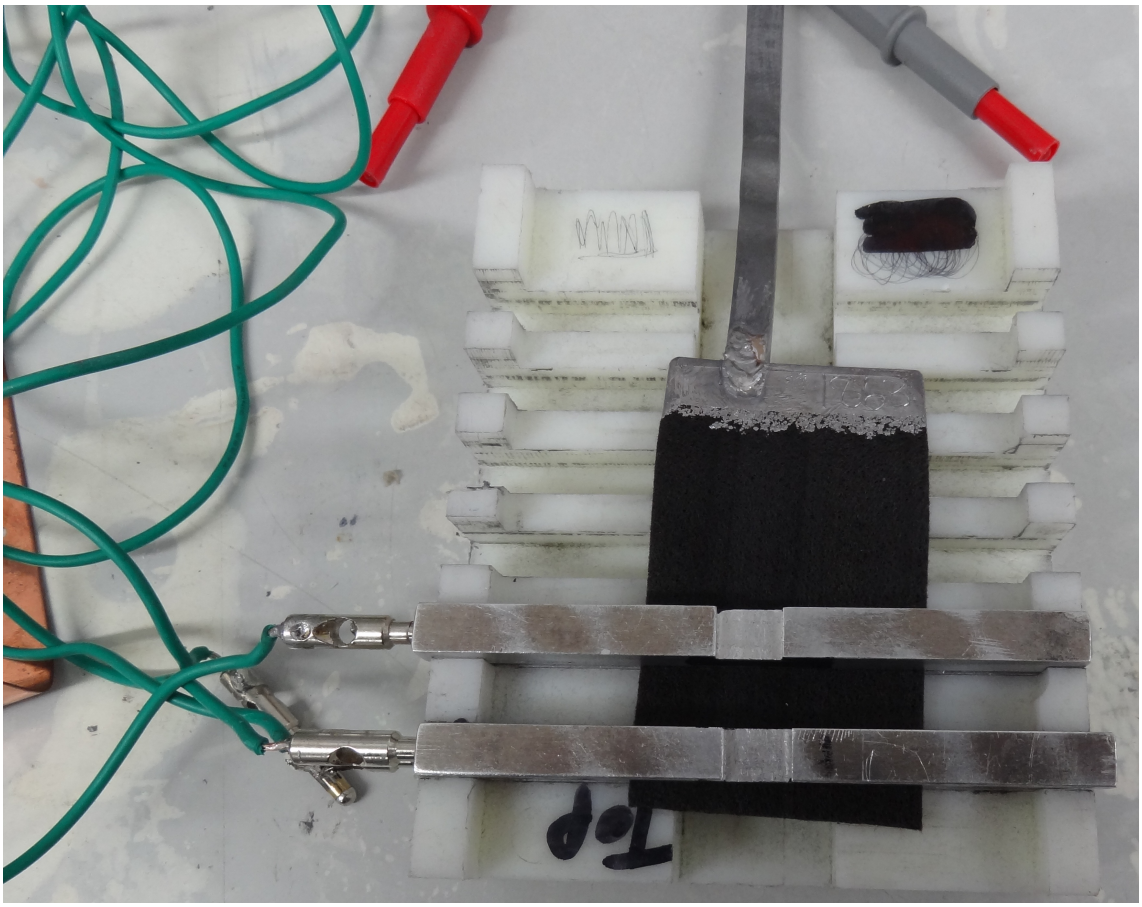

Figure 1: Resistivity measuring jig

.3 Thermal conduction through composite system

The system is a non–polarizable ellipsoid suspended in solution between two electrode plates. The force acting on the suspended particle is composed of the electric force V, due to the surface charge of the electrodes, and the mean value of the forces due to the surface charge on the suspended particles throughout the whole space of the suspending medium.

Fricke then develops the equations describing this force, using confocal co–ordinates which gives the force as

$$V_x = -F_x = -F\sqrt{\frac{(a^2+\lambda)(a^2+\mu)(a^2+v)}{(b^2-a^2)(c^2-a^2)}} \tag{1}$$

The electrical conductivity can be found from this force by dividing the suspension into integral sized spacing. Through the use of boundary conditions and Ohm's law Fricke gets

$$k = k_1 + \frac{\frac{1}{3}\rho}{1-\rho} \sum^{x=a,b,c} \frac{2(k_2 - k)}{2 + abcL_a(k_2/k_1 - 1)} \tag{2}$$

where

k = conductivity of the suspension

k_1 = conductivity of the suspending medium

k_2 = conductivity of the suspended ellipsoids

ρ = ratio of the densities of the the medium and ellipsoids

L_a = the definite integral of the force along the x axis through the ellipsoid

solving for the integral gives

$$k = k_1 + \frac{k_1 \rho \beta}{(1-\rho)} \frac{(k_2 - k)}{(k_2 - k_1)} \tag{3}$$

where β is a geometrical factor. For the case of a spheroid with b $\ggg$ a equation 3 can be simplified and rearranged to give